Article

Cell

Prefrontal Parvalbumin Neurons in Control of Attention

Graphical Abstract

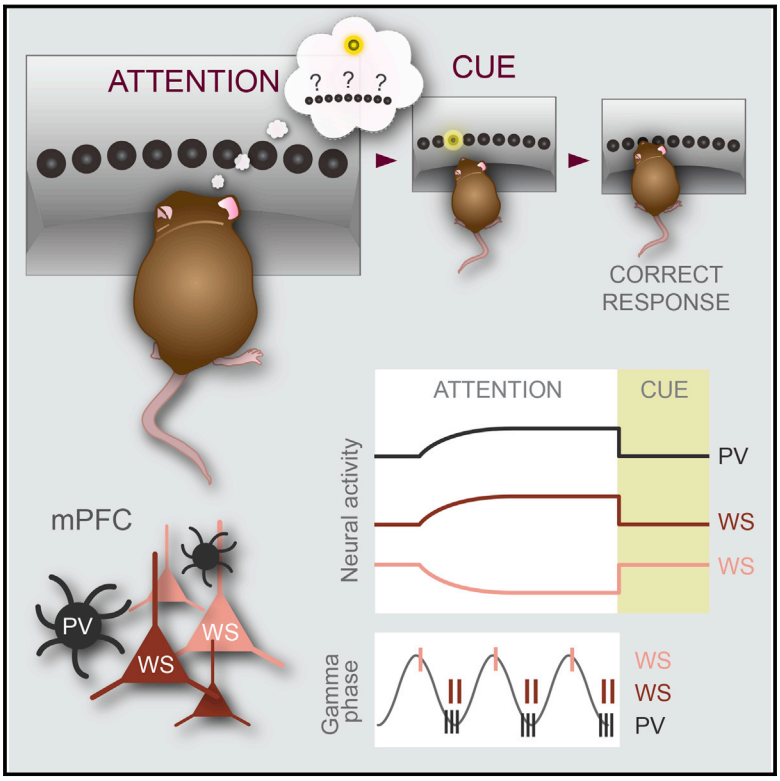

Authors

Hoseok Kim, Sofie Ährlund-Richter, Xinming Wang, Karl Deisseroth, Marie Carlén

Correspondence

marie.carlen@ki.se

In Brief

A combination of electrophysiology and optogenetic manipulations reveal that inhibitory parvalbumin interneurons and gamma oscillations are central to prefrontal cortex's control of attention.

Highlights

- Increased firing of mPFC PV interneurons is a signature of top-down attention
- Attention is characterized by synchronization of mPFC PV neurons and elevated gamma
- Local pyramidal neurons show gamma-phase-dependent rate modulation during attention
- Synchronization of mPFC PV neurons at gamma frequencies has pro-cognitive effects

Kim et al., 2016, Cell *164*, 208–218
January 14, 2016
http://dx.doi.org/10.1016/j.cell.2015.11.038

CellPress

Cell

Article

Prefrontal Parvalbumin Neurons in Control of Attention

Hoseok Kim,[1] Sofie Ährlund-Richter,[1] Xinming Wang,[1] Karl Deisseroth,[2,3,4] and Marie Carlén[1,*]
[1]Department of Neuroscience, Karolinska Institutet, Retzius väg 8, 171 77 Stockholm, Sweden
[2]Howard Hughes Medical Institute
[3]Department of Bioengineering
[4]Department of Psychiatry and Behavioral Sciences
W080 Clark Center, 318 Campus Drive West, Stanford University, Stanford, CA 94305, USA
*Correspondence: marie.carlen@ki.se
http://dx.doi.org/10.1016/j.cell.2015.11.038

SUMMARY

While signatures of attention have been extensively studied in sensory systems, the neural sources and computations responsible for top-down control of attention are largely unknown. Using chronic recordings in mice, we found that fast-spiking parvalbumin (FS-PV) interneurons in medial prefrontal cortex (mPFC) uniformly show increased and sustained firing during goal-driven attentional processing, correlating to the level of attention. Elevated activity of FS-PV neurons on the timescale of seconds predicted successful execution of behavior. Successful allocation of attention was characterized by strong synchronization of FS-PV neurons, increased gamma oscillations, and phase locking of pyramidal firing. Phase-locked pyramidal neurons showed gamma-phase-dependent rate modulation during successful attentional processing. Optogenetic silencing of FS-PV neurons deteriorated attentional processing, while optogenetic synchronization of FS-PV neurons at gamma frequencies had pro-cognitive effects and improved goal-directed behavior. FS-PV neurons thus act as a functional unit coordinating the activity in the local mPFC circuit during goal-driven attentional processing.

INTRODUCTION

Attention plays a crucial role in our ability to organize thoughts and actions in meaningful behavior. On a neurophysiological level, attention biases processing of certain neural representations at the expense of others. As a result, behaviorally relevant information is amplified, while distracting or irrelevant information is suppressed (Noudoost et al., 2010). The prefrontal cortex (PFC) directly influences attentional processing (Baluch and Itti, 2011; Clark et al., 2015; Gregoriou et al., 2014; Miller and Buschman, 2013; Moore and Armstrong, 2003; Zhang et al., 2014), but the local computations underlying PFC's control of attention have not been established. Cortical inhibitory interneurons expressing parvalbumin (PV) are powerful regulators of local network activities (Hu et al., 2014), and synchronous activation of PV neurons is sufficient for induction of gamma oscillations (30–80 Hz) (Buzsáki and Wang, 2012; Cardin et al., 2009; Sohal et al., 2009). PV neurons in sensory areas contribute to the signatures of attention through local modulation of sensory responses (Atallah et al., 2012; Lee et al., 2012; Wilson et al., 2012), including through the expression of gamma oscillations (Siegle et al., 2014). Importantly, attentional processing is characterized by increases in gamma activity, both in sensory as well as prefrontal areas (Gregoriou et al., 2014) (Gregoriou et al., 2015).

Activity of cortical PV neurons is not only essential for microcircuit operations but does also correlates to behavioral events (Isomura et al., 2009; Kvitsiani et al., 2013), and recent findings suggest that prefrontal PV neurons can act as a functional unit able to orchestrate the flow of information in and between brain areas (Courtin et al., 2014; Kepecs and Fishell, 2014). Given the functional repertoire of PV neurons, it is not surprising that this neuronal cell type repetitively has been implicated in a variety of neurological and psychiatric diseases (Marín, 2012). The links are especially strong in schizophrenia, a disabling mental disorder with well-defined impairments in the control of attention (Lustig et al., 2013). Patients with schizophrenia demonstrate impairment in visual search when top-down goals are required, showing a selective deficit in top-down control of attention (Gold et al., 2007). Cognitive deficits in schizophrenia are suggested to emerge from impaired prefrontal gamma oscillations (Lewis et al., 2012), and the key role of PV neurons in the generation of cortical gamma oscillations links this neuronal class to cognitive deficits (Carlén et al., 2012; Korotkova et al., 2010).

Despite many intersecting lines of circumstantial evidence, proof for a function of inhibitory medial PFC (mPFC) PV neurons in the control of attention is lacking. Moreover, it is yet to be demonstrated how cortical PV neurons relate to gamma activity in attention and how prefrontal gamma oscillations could contribute to the behavioral benefits of attention. Elucidation of the circuit underpinnings of top-down control of attention will not only give answers to central questions regarding how PFC contributes to purposeful behavior, but will also give insight on how circuit disturbances could underlie symptomatology in mental disorders characterized by altered cognition.

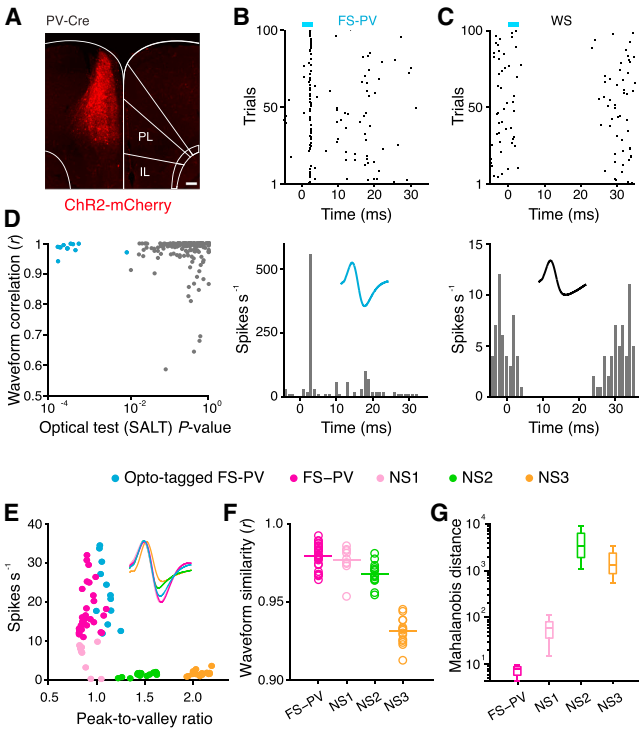

Figure 1. Optogenetic Tagging and Classification of mPFC FS-PV Neurons in Freely Moving Mice

(A) Expression of ChR2-mCherry (red) in mPFC FS-PV neurons in a PV-Cre mouse injected unilaterally with AAV DIO ChR2-mCherry. (n = 4 PV-Cre mice). PL, prelimbic; IL, infralimbic. Scale bar, 100 μm.

(B and C) Raster plot (top) and peri-stimulus time histogram (PSTH; bottom) of a light-activated FS-PV neuron (B) and an inhibited WS neuron recorded from the same tetrode (C), both aligned to light onset. Insets display representative spike waveforms.

(D) Scatter plot of SALT versus waveform correlation for identification of directly light-activated neurons (n = 252 analyzed neurons). Optically tagged neurons (n = 12, $p < 0.01$ by SALT; blue) display high waveform correlation between light evoked and spontaneous spikes ($r > 0.9$).

(E) Scatter plot of firing rate versus peak-to-valley ratio for opto-tagged FS-PV units and all recorded NS units. Opto-tagged FS-PV units (blue) cluster with FS-PV neurons identified by electrophysiological properties (purple). Inset displays representative spike waveforms.

(F) Waveform similarity between opto-tagged FS-PV and recorded NS neurons. $r = 1.0$: a waveform identical to the waveform of opto-tagged FS-PV neurons.

(G) Mahalanobis distance between the cluster of opto-tagged FS-PV neurons and clusters of recorded NS neurons.

See also Figure S2.

RESULTS

Identification and Recording of mPFC Neurons during Top-Down Control of Attention

To characterize the recruitment and firing modulation of mPFC neurons during attentional processing, we conducted chronic electrophysiological recordings in mice performing a three-choice version of the five-choice serial reaction time task (5-CSRTT) (Robbins, 2002). The 5-CSRTT is a widely employed rodent attention task, building on tests of sustained attention originally developed for humans, and is identified as having high construct validity (Lustig et al., 2013). In the task, animals are required to orient to an array of stimulus presentation holes in an operant chamber and to allocate attention to detect and report the location of a brief visual stimulus (cue) presented pseudorandomly in one of three presentation holes (Figure S1A and Movie S1). The animals were subjected to a six-step training schedule defined by specific criteria (modified from Bari et al. [2008]) (Figures S1B–S1F) to fully learn the task (n = 28 ± 8 training days for all animals used, n = 13 PV-Cre mice). After meeting the target criteria, three PV-Cre mice were implanted with microdrives holding four movable tetrodes targeted to prelimbic (PL) and infralimbic (IL) cortex (Figures S2A–S2C), and 426 well-isolated neurons were recorded during 3-CSRTT (54 sessions, 3,857 trials in total). As a first step, we classified the recorded units into narrow-spiking (NS; n = 70, half-valley width 252 ± 36 μs) putative inhibitory interneurons and wide-spiking (WS; n = 329, half-valley width 428 ± 37 μs) putative pyramidal neurons based on spike waveform features (Stark et al., 2013; Figure S2D). Units with low classification confidence ($p > 0.05$, n = 27) were not classified. The waveform classification revealed three potential NS clusters, and the units were therefore further classified based on firing rate (Figure S2E). This parameter identified a population of fast-spiking NS neurons, and NS units with an average firing rate > 10 Hz were classified as FS-PV neurons (n = 30, mean firing rate 18 ± 6 Hz, all data from all trials). Inhibitory interactions and short-latency suppression of WS spiking were confirmed for 21 of the 30 FS-PV neurons in computed cross-correlograms (Fujisawa et al., 2008; see further below).

Optogenetics enables verification of physiology-based classification of neurons recorded in vivo (Kvitsiani et al., 2013; Roux et al., 2014), and we therefore paired chronic extracellular recordings with optical tagging of FS-PV neurons in freely moving animals (n = 4 PV-Cre mice, 46 opto-tagging sessions). An adeno-associated virus expressing channelrhodopsin-2 (ChR2) (Cardin et al., 2009) was targeted to mPFC to render PV neurons sensitive to blue light (Figure 1A). Application of blue light (473 nm, 5 mW, 3–5 ms light pulses, 10–90 Hz) elicited short-latency action potentials in ChR2-expressing FS-PV neurons followed by inhibition of WS neurons recorded on the same tetrode (Figures 1B and 1C), demonstrating efficient temporal control of FS-PV neuron activity during active behavior. Using stimulus-associated spike latency test (SALT) in combination with a spike-shape correlation measure (Kvitsiani et al., 2013), we confirmed that the 12 units optically tagged and recorded were directly light-driven FS-PV neurons (Figure 1D). Comparison of the electrophysiological properties between NS neurons recorded during 3-CSRTT and FS-PV neurons identified through opto-tagging confirmed that our physiological classification correctly categorized FS-PV neurons (Figures 1E–1G).

FS-PV Neurons, but Not WS Neurons, Closely Track Attention

The 3-CSRTT assesses attentiveness to multiple locations and the speed of processing over a large number or trials. Incorrect reporting of stimulus location (nose-poke response into wrong hole; Movie S3), premature reporting (nose-poke response before cue onset; Movie S2), and omission (failure to report

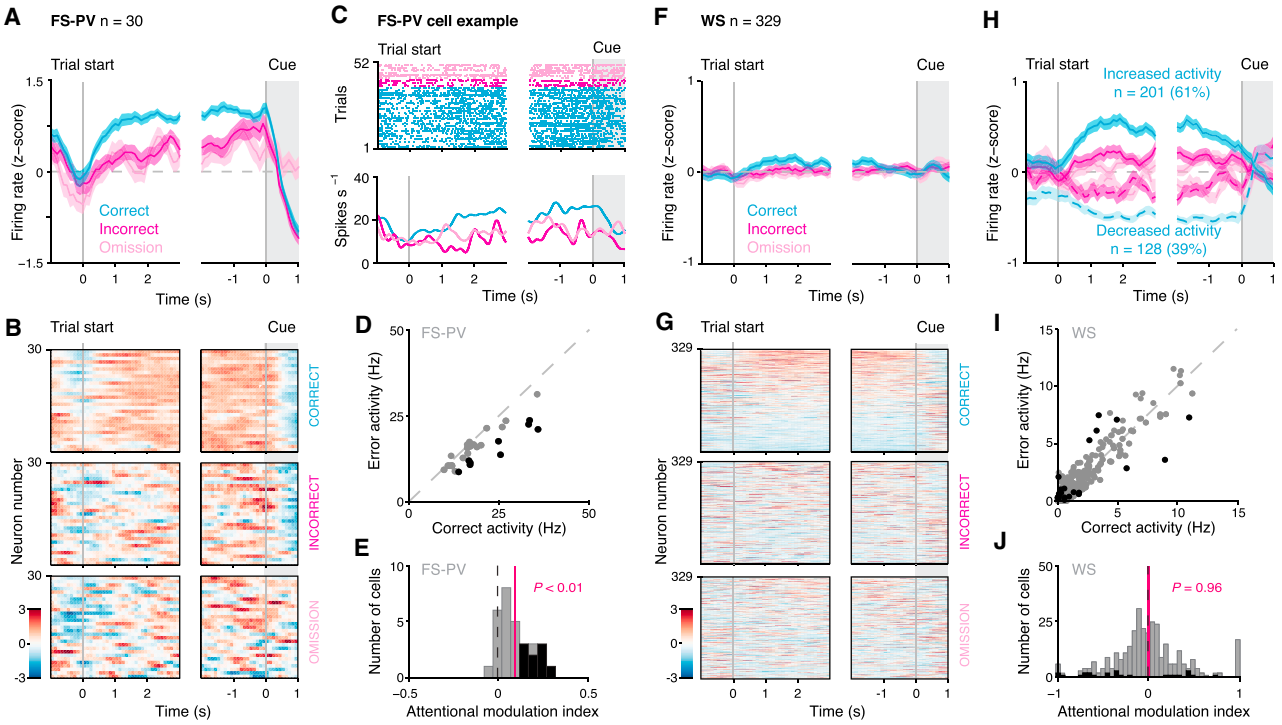

Figure 2. Firing Modulation of mPFC FS-PV and WS Neurons during Attentional Processing

(A–C) and (F–H) PETH aligned to trial start and to cue onset for all FS-PV (n = 30) and WS neurons (n = 329) recorded in the 3-CSRTT. The timeline is broken due to the pseudorandom delay. 500 ms sliding window, 100 ms time bins.

(A) Mean *Z* scores of responses of the whole FS-PV population based on the behavioral outcome of the trials (correct, blue; incorrect, purple; omission, pink). Shaded areas, SEM.

(B) Individual mean *Z* scores of all recorded FS-PV neurons. The neurons are plotted in the same order for the three behavioral outcomes with the colors indicating low (blue) to high (red) firing rate.

(C) Spike raster (top) and spike density functions (a guassian kernel σ = 100 ms; bottom) of an example FS-PV neuron based on the behavioral outcome of each trial; colors as in (A).

(D) Comparison of the average firing rate of the recorded FS-PV neurons in correct versus error (incorrect + omission) trials, 1 s (−1 to 0 s) before cue onset. 9 out of 30 FS-PV neurons display a significantly increased firing rate in correct trials (black dots; $p < 0.05$, Wilcoxon rank-sum test).

(E) Attentional modulation index of the FS-PV population (red line; 0.1 ± 0.09, mean ± SD; $p < 0.01$, t test). 30% of the individual neurons are significantly modulated by attention (black; $p < 0.05$, Wilcoxon rank-sum test). Positive values refer to enhanced spiking in correct trials, and negative values refer to enhanced spiking in error trials.

(F) Mean *Z* scores of responses of the whole WS population based on the behavioral outcome of the trials. Colors as in (A); shaded areas, SEM.

(G) Individual mean *Z* scores of all recorded WS neurons. The neurons are plotted in the same order for the three behavioral outcomes with the colors indicating low (blue) to high (red) firing rate.

(H) Mean *Z* scores of responses of all WS neurons based on behavioral outcome and on whether a neuron displays a mean increased or decreased activity during the delay of correct trials (blue). This dissociates the neurons into one population with increased activity (solid line) and one population with decreased activity (dashed line). The two populations display less dissociated activities during incorrect (purple) and omitted (pink) trials. Shaded areas, SEM.

(I) Comparison of the average firing rate of the recorded WS neurons in correct versus error (incorrect + omission) trials 1 s (−1 to 0 s) before cue onset. 9 out of 329 neurons (2.7%) show significantly increased activity in correct trials and 16 out of 329 neurons (4.9%) in error trials (black dots; $p < 0.05$, Wilcoxon rank-sum test).

(J) Attentional modulation index of the WS population (red line; 0.0 ± 0.4, mean ± SD; $p = 0.96$, t test). Colors as in (E).

See also Figures S1 and S3.

cue location within a defined time span; Movie S4) are scored as errors and are considered to reflect disturbances in attentional processing and executive functioning (Robbins, 2002). To increase the attentional load and prevent self-pacing strategies for prediction of stimulus onset, we employed pseudorandom delays ("delay" refers to time from trial start to cue onset) with the cue being presented 3, 4, or 5 s after trial start, on a trial-to-trial basis ("event onset asynchrony").

We focused our examination of the responses of the recorded FS-PV and WS populations to the delay (i.e., when attention is allocated [Totah et al., 2009, 2013; Figure S1A]). The firing rate modulation was analyzed based on the behavioral outcome (correct, incorrect, or omitted response). Premature responses cancel cue presentation, and we therefore did not perform analysis of recordings from trials with this type of error. Trial start was reported by an increase in FS-PV activity, independent of behavioral outcome (Figure 2A). However, in trials with correct report of cue location, the FS-PV neurons uniformly displayed a sustained enhancement of firing during the delay compared to trials with incorrect report or omission (Figures 2A–2D). Already 300 ms

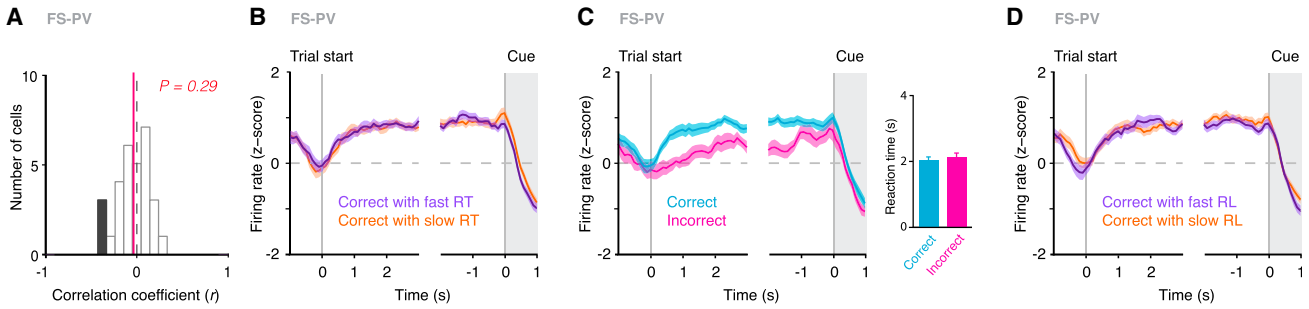

Figure 3. The mPFC FS-PV Activity Correlates to Attentional Processing

(A–D) FS-PV neurons, n = 30.

(A) There is no correlation between the FS-PV activity (−1 to 0 s before cue onset) and the reaction time (RT) in correct trials (red line; $r = 0.04 \pm 0.19$, mean ± SD; p = 0.29, t test). Black indicates significance ($p < 0.05$).

(B) FS-PV activity during attentional processing in correct trials based on the RT (slow or fast).

(C) FS-PV activity during attentional processing for correct and incorrect trials with similar RT.

(D) FS-PV activity during attentional processing in correct trials based on the latency to collect reward (RL; slow or fast).

Shaded areas, SEM. See also Figure S4.

after trial start, the FS-PV activity was significantly higher in correct trials compared to error trials (incorrect + omission). It was thus possible, based on the level of the FS-PV activity, to predict successful behavior (i.e., correct response) more than 2.5 s before cue onset ($p < 0.05$, paired t test, example from shortest delay [3 s]). As a population, the FS-PV neurons showed a remarkably homogenous firing rate modulation during the delay preceding a successful behavioral response (Figure 2B), with up to 40% of the neurons displaying significantly elevated firing rates in correct trials (Figure S3A). As a whole, the FS-PV activity was modulated by attention (Figure 2E).

Analysis of the firing rate of the WS population (n = 329) revealed only minor modulations throughout the delay, regardless of behavioral outcome (Figure 2F). Yet, the elevated FS-PV firing is expected to exert pronounced inhibitory effects on local WS spiking (Hu et al., 2014; Roux and Buzsáki, 2015). In support of this, we found a high prevalence of short-latency inhibitory putative monosynaptic interactions between FS and WS neurons in computed cross-correlograms (Fujisawa et al., 2008), identifying functional connectivity between the cell types and FS-PV suppression of WS spiking (Figure S3B). We therefore next analyzed the firing rate modulation during the delay of correct trials for each WS neuron individually (Figures 2G and S3C). Interestingly, this revealed a clear dissociation of the WS population, with 61% of the WS neurons showing elevated activity and 39% suppressed activity (Figures 2G and 2H). Mixed modulation of mPFC activity during attentional processing has been observed in the 3- and 5-CSRTT in earlier studies, in which the recorded neurons were not classified into cell types (Donnelly et al., 2015; Totah et al., 2009). Importantly, the WS sub-population with enhanced activity in correct trials displayed lower firing rates in error trials (Gregoriou et al., 2014; Figure 2H). Conversely, the WS subpopulation with suppressed activity in correct trials was less suppressed in error trials (Figure 2H). In line with this, the strongest and fastest inhibition by FS-PV neurons was seen in correct trials, targeting the WS sub-population with suppressed activity (trough at 3 ms in correct trials and 4 ms in error trials for WS neurons with suppressed activity; Figure S3D). Taken together, WS neurons showed mixed activities during attentional processing (Figures 2I and S3E), but the WS activity as a whole was not modulated by attention (Figure 2J).

The response latency (i.e., the reaction time: time from cue onset to nose-poke response) correlated to trial outcome, corroborating previous findings (Totah et al., 2009), with faster responses in correct trials compared to incorrect trials (correct: 1.7 ± 0.3 s; incorrect: 2.1 ± 0.5 s, $p < 0.01$, paired t test), even during training (Figure S1F). Interestingly, there was no correlation between the reaction time and the FS-PV activity directly before cue onset in correct trials (i.e., the time point when the animals most urgently must allocate attention in order to not miss the presentation of the cue [Figure 3A]). Further, the pattern of FS-PV activity was indistinguishable between correct trials with fast and slow reaction times (Figure 3B). These findings suggest that the recorded FS-PV activity does not correlate to general task engagement (Hayden et al., 2009) or motor preparation. In support of this, the FS-PV activity was modulated differently in correct and incorrect trials with very similar reaction times (i.e., although the behavioral responses were performed with very similar latencies, the FS-PV activity clearly reflected the respective trial type's level of attention and predicted the outcome of the behavior [Figure 3C]).

Analysis of the latency to collect reward after correct responses (reward collection latency, RL; Figure S1A) provides a sensitive control measure of motivation, with longer reward latencies reflecting lowered motivation (Robbins, 2002). We found that the FS-PV activity during attentional processing in correct trails with fast reward latencies was not different from the activity in correct trials with slow reward latencies, arguing against the recorded FS-PV activity being a correlate of the motivational state of the animal (Figure 3D). Collectively, these findings lend support to the interpretation that elevated and sustained mPFC FS-PV delay activity is a correlate of successful attentional processing.

Error or reward processing could potentially influence the neuronal activity in a subsequent trial, and we therefore investigated how the FS-PV activity during the delay was affected by

the outcome of previous behavior (i.e., if the previous trial was rewarded or not). The level of FS-PV activity during the delay of trials with correct responses was very similar, regardless of whether the previous trial was rewarded or not, with the distinction that the elevation of activity came significantly earlier if the previous trial had been rewarded ($p < 0.01$, paired t test; Figure S4). This suggests that the consequence of the animal's previous behavior does not affect the level of recruitment of mPFC FS-PV neurons but possibly influences the timing of recruitment.

Successful Allocation of Attention Is Characterized by Synchronization of mPFC FS-PV and WS Neurons and Enhanced Gamma Oscillations

Allocation of attention is correlated to enhancement of gamma synchronization in PFC (Gregoriou et al., 2009, 2015), and it has been proposed that oscillations in the gamma range benefit cortical processing and behavior (Fries, 2009; Pritchett et al., 2015). Analysis of the local field potential (LFP) revealed distinct bouts of spontaneously occurring gamma during the delay in trials with correct responses (Figure 4A). The 30–40 Hz gamma activity was significantly elevated in correct trials compared to trials with omitted responses. Trials with incorrect report of cue location showed intermediate levels of gamma activity, possibly reflecting the notion that attention is indeed engaged in incorrect trials, but not sufficiently to support correct report of the cue location (Totah et al., 2009; Figures 4B–4D). Importantly, the gamma amplitude did not differ between trial types directly after termination of the delay (i.e., the elevation of gamma in correct trials was specific to the time point when attention was allocated [Figures 4D and 4E]).

Optogenetics has provided causative in vivo evidence for the crucial role of FS-PV neurons in the emergence of cortical gamma oscillations; ChR2 drive of FS-PV neurons at gamma frequencies entrain naturalistic gamma in the local in vivo circuit (Cardin et al., 2009; Siegle et al., 2014; Sohal et al., 2009). To infer whether gamma activity coupled to attention depends on synchronous firing of mPFC FS-PV neurons, we investigated the alignment and level of phase locking of FS-PV firing during the last 2 seconds of the delay. The FS-PV population was significantly phase locked (Vinck et al., 2013) and fired in the same phase (the trough) of the gamma cycle in all types of trials, with strongest phase locking in correct trials (i.e., during successful allocation of attention characterized by elevated gamma activity [Figure 4F]). Selective investigation of significantly phase-locked FS-PV neurons revealed a strong phase concentration of the spiking in the trough of the gamma cycle (Siegle et al., 2014) in correct trials (Figure 4G). This pronounced synchronous FS-PV firing was followed by a period of suppressed local WS firing (Figures 4H and 4I). Further, in correct trials, the WS firing became significantly phase locked to gamma (Figures 4H and 4I). This characteristic pattern and alignment of FS-PV phase-locking are consistent with the dynamics of FS-PV-driven gamma (Pritchett et al., 2015 but see Buzsáki and Wang, 2012). Taken together, successful allocation of attention was characterized by gamma-rhythmic inhibition by FS-PV neurons, increased temporal precision of WS firing, and synchronization of WS firing (Hasenstaub et al., 2005).

Differential Attentional Modulation of WS Neurons Phase Locked to Local Gamma

A closer look at the phase distributions revealed that WS neurons phase locked to gamma during successful allocation of attention (i.e., in correct trials) preferentially fired in either the trough or at the peak of the gamma cycle (Figure 4I). In addition to temporally sharpening WS responses (Cardin et al., 2009; Hasenstaub et al., 2005) and increasing synchronization, gamma-rhythmic inhibition by FS-PV neurons is implicated in gating of inputs and in gain control (Tiesinga et al., 2004, 2008), with the phase of gamma influencing the efficacy by which excitatory inputs drive local WS responses (Womelsdorf et al., 2014). Optogenetic experiments have shown that synaptic inputs arriving in the trough of gamma (i.e., when the level of inhibition is lowest) evoke enhanced responses of local WS neurons, while inputs arriving in the opposite phase evoke diminished responses (Cardin et al., 2009; Siegle et al., 2014). To directly investigate a potential relationship between endogenous gamma activity and responses of local mPFC WS neurons during attention, we selectively analyzed the firing rates during the delay of the WS neurons significantly phase locked to the trough or the peak of the gamma cycle in correct trials (Figures 5A and 5B). Interestingly, this separated the WS neurons into two sub-populations, with WS neurons discharging in the trough of gamma displaying increased firing and WS neurons discharging at the peak displaying suppressed firing (Figure 5C).

Top-Down Control of Attention Relies on FS-PV Activity

The strong network and behavioral correlate of mPFC FS-PV activities imply a functional role of this population in top-down control of attention and goal-directed behavior. In order to directly address this hypothesis, we employed optogenetic silencing of the FS-PV neurons during the delay. Light-activated inhibiting chloride-conducting channels were recently developed through structure-guided transformation of an originally cation-conducting channelrhodopsin (Berndt et al., 2014). Inhibitory channels hold several advantages over the traditionally used inhibitory pumps, including a more physiological inhibition of action potentials. SwiChR is a fast and bistable inhibitory step-function channel that can be used for inhibition of neuronal spiking for seconds (Berndt et al., 2014). Brief blue light application results in stable inhibition that can be terminated by application of red-shifted light. To confirm the bistable inhibitory action of SwiChR in vivo, we performed recordings in prelimbic/infralimbic cortex of PV-Cre mice injected with AAV DIO SwiChR-EYFP (n = 4 PV-Cre mice; Figure S5A). Blue light application (1 s, 473 nm, 5 mW) inhibited FS-PV spiking, resulting in disinhibition of neurons in the local circuit for several seconds, which could be counteracted by application of red light (1 s, 638 nm, 5 mW; Figures S5B–S5D). We expressed SwiChR bilaterally in mPFC PV neurons (Figures 6A and 6B) in trained animals (n = 5 PV-Cre mice) and pseudorandomly silenced the mPFC PV neurons' activity during the delay in 50% of the trials (total number of trials: 4,362). In separate sessions, 0.5, 1.0, or 2.0 s pulses of blue light (473 nm, 5 or 7 mW) were used (for experimental outline, see Figure S1A). Inhibition of FS-PV activity was terminated with 1 s of red light (638 nm; 5 mW) directly after the delay in all trials with SwiChR application. In essence,

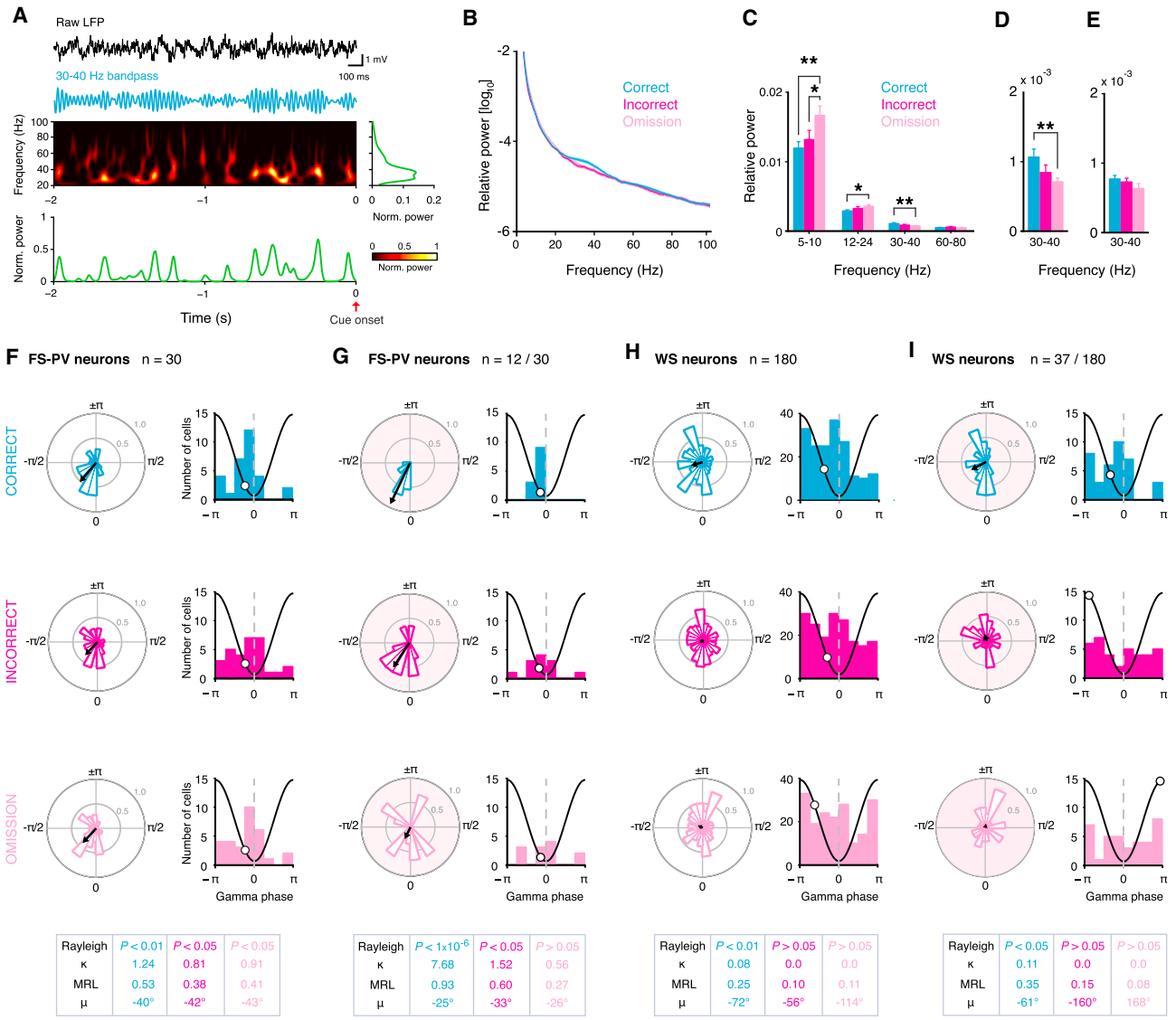

F	Rayleigh	$P < 0.01$	$P < 0.05$	$P < 0.05$
	κ	1.24	0.81	0.91
	MRL	0.53	0.38	0.41
	μ	-40°	-42°	-43°

G	Rayleigh	$P < 1x10^{-6}$	$P < 0.05$	$P > 0.05$
	κ	7.68	1.52	0.56
	MRL	0.93	0.60	0.27
	μ	-25°	-33°	-26°

H	Rayleigh	$P < 0.01$	$P > 0.05$	$P > 0.05$
	κ	0.08	0.0	0.0
	MRL	0.25	0.10	0.11
	μ	-72°	-56°	-114°

I	Rayleigh	$P < 0.05$	$P > 0.05$	$P > 0.05$
	κ	0.11	0.0	0.0
	MRL	0.35	0.15	0.08
	μ	-61°	-160°	168°

Figure 4. Successful Allocation of Attention Is Characterized by Synchronization of mPFC FS-PV and WS Neurons and Enhanced Gamma Oscillations

(A–D) and (F–I) Data from the last 2 s of the delay.

(A) Raw LFP, band-pass filtered LFP (30–40 Hz), and spectrogram (20–100 Hz) from a correct trial, including the average power (right green trace) and average 30–40 Hz band power (bottom green trace) of the spectrogram.

(B) Average relative LFP power (1–100 Hz) based on behavioral outcome. Shaded areas, SEM.

(C) Average relative LFP power in different frequency bands. The activity in the gamma band (30–40 Hz) is significantly elevated during successful allocation of attention (correct trials, blue) compared to trials with omission (pink); $p < 0.01$, paired t test. Error bars, mean ± SEM.

(D) Close-up of the 30–40 Hz activity in (C).

(E) 30–40 Hz activity directly after termination of the delay (i.e., during the cue; 0 to 1 s after cue onset). The level of gamma does not differ between trial types ($p > 0.1$, one-way ANOVA with repeated measures). Error bars, mean ± SEM.

(F–I) (Left) Circular distribution of the mean-spike gamma-phase angles (15° bin width) based on behavioral outcome. (Black arrow) Direction and magnitude (length) of the MRL for the population (MRL, 1.0 = exact phase synchronization of the neurons). (Right) Distribution of mean-spike gamma-phase angles (45° bin width) based on behavioral outcome. (Black line) One schematic gamma cycle. (White circle) Mean phase angle (μ). (Bottom) Table with population-phase-locking statistics. κ = circular concentration coefficient.

(F) Data for FS-PV neurons with ≥ 50 spikes during the last 2 s of the delay (n = 30; i.e., all FS-PV neurons).

(G) Data for FS-PV neurons with ≥ 50 spikes during the last 2 s of the delay and significant phase locking to gamma in correct trials ($p < 0.05$, Rayleigh test, n = 12 / 30). The firing of FS-PV neurons is most synchronized in correct trials (peak at 26.5 ± 1.7 ms, 30–40 Hz gamma).

(H) Data for WS neurons with ≥ 50 spikes during the last 2 s of the delay (n = 180).

(I) Data for WS neurons with ≥ 50 spikes during the last 2 s of the delay and significant phase locking to gamma in correct trials ($p < 0.05$, Rayleigh test, n = 37 / 180). This WS population becomes phase locked to gamma in correct trials (peak at 23.7 ± 5.2 ms, 30–40 Hz gamma).

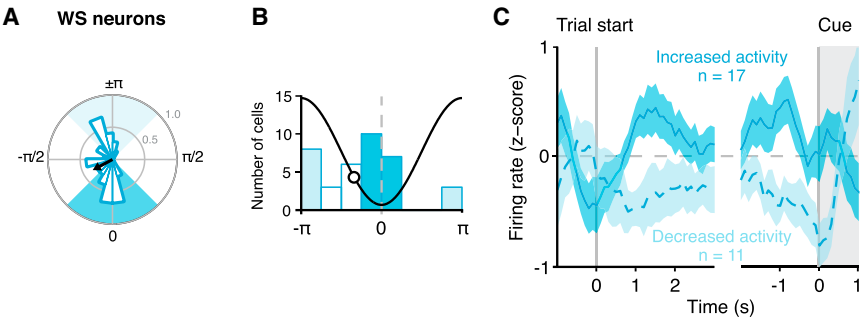

Figure 5. Gamma-Phase Modulation of WS Firing during Successful Allocation of Attention

(A–C) Data from correct trials, (A and B) same data as Figure 4I correct trials.

(A) Polar chart with color-coded gamma phases: blue, −45° to 45° refers to the trough of the gamma cycle; light blue, −135° to 135° refers to the peak of the gamma cycle. Circular distribution of the mean-spike gamma-phase angles (15° bin width) of the 37 WS neurons with ≥ 50 spikes during the last 2 s of the delay and significant phase locking to gamma in correct trials ($p < 0.05$, Rayleigh test).

(B) Distribution of mean-spike gamma-phase angles (45° bin width) for the neurons in (A). Colors as in (A).

(C) Firing modulation during the delay of the WS neurons in (B), firing in the trough (blue and solid line) or at the peak (light blue and dashed line) of the gamma cycle. Shaded areas, SEM.

we ensured that inhibition of FS-PV spiking matched the temporal pattern of elevated FS-PV activity during successful allocation of attention.

Inhibition of FS-PV neurons during attentional processing resulted in more than a doubling of the total number of errors (premature + incorrect + omission), regardless of blue light-pulse duration ($p < 0.01$, paired t test; Figure 6C). The major effect seen was a large increase in the number of omitted trials ($p < 0.01$, paired t test; Figures 6D and S6A). Omissions can reflect inattentiveness, particularly in mice, which are prone to withhold a response after failure to attend to the stimulus (Amitai and Markou, 2010). To investigate this further, we analyzed deficits in other domains. Analysis of the latency to collect reward after correct responses revealed that SwiChR silencing of mPFC FS-PV neurons did not affect reward latencies, independent of blue light-pulse duration and power intensity (Figures S6B and S6C), arguing against a general effect on internal motivation (Robbins, 2002).

Increased omissions could theoretically be attributed to deficits in motor activity (Robbins, 2002). Deficits in motor activity would be expected to be consistent in trials with SwiChR activation and, thus, independent of trial outcome, and we therefore analyzed the response latency (i.e., the reaction time) for correct responses. SwiChR application did not result in increased response latencies in correct trials with light application compared to correct trials without light, independent of blue-light-pulse duration and light intensity (Figures S6D and S6E). Together, these findings lend support to the notion that silencing of mPFC FS-PV activities during the delay selectively disrupts attentional processing.

Frequency-Dependent FS-PV Modulation of Attention

Optogenetic activation of cortical PV neurons has been employed in many studies investigating cortical computations (for review, see Hangya et al., 2014; Kepecs and Fishell, 2014; Roux et al., 2014). Optogenetic drive of FS-PV activity can, depending on the stimulation paradigm used and the network operations affected, lead to both perturbation (Sachidhanandam et al., 2013; Siegle et al., 2014) and enhancement (Lee et al., 2012; Siegle et al., 2014) of ongoing network activities and, ultimately, influence behavior (Pritchett et al., 2015). To directly investigate how synchronization of FS-PV firing at different frequencies influences attentional processing, we expressed ChR2 bilaterally in mPFC FS-PV neurons in a cohort of animals trained in the 3-CSRTT (n = 5 PV-Cre mice; Figures 7A and 7B). Blue light (473 nm, 3 ms light pulses, 5 or 7 mW) was applied throughout the pseudorandom delay (3, 4, or 5 s) or during the last 2 seconds of the delay pseudorandomly in 50% of the trials (total number of trials: 10,302; for experimental outline, see Figure S1A). Interestingly, optogenetic activation of FS-PV neurons at frequencies lower (1–10 Hz) than the native FS-PV activity displayed in correct trials directly before cue onset (19.25 ± 7.55 Hz, −1 to 0 s before cue onset) resulted in a significant increase in the total number of errors (premature + incorrect + omission; $p < 0.01$ paired t test; Figures 7C and S7A). As with the use of SwiChR, there was a large increase in the number of omitted trials ($p < 0.01$ paired t test; Figures 7D and S7B), but also the number of premature responses was increased with light application throughout the delay. Premature responses are thought to reflect deficits in impulse control, a PFC-dependent cognitive trait tightly linked to attentional processing. The negative effect on the behavior implies that intermittent forced synchronization of FS-PV neurons at low frequencies disrupts ongoing local network activities supporting attention. Our data further indicate that attention works in concert with response inhibition and that the two functions might share network underpinnings.

Activation at 20 Hz (i.e., close to the native FS-PV rate displayed before the cue in correct trials) did not change the error rate ($p > 0.1$, paired t test; Figures 7C, 7D, S7A, and S7B), indicating that synchronization of FS-PV activity per se does not disrupt attention. Despite extensive training, the animals do not correctly report the cue location in 100% of the trials. The most common error is an omission (Figures 6D and 7D), which presumably depends on a natural inability to sustain attention in every trial of a session. Improvement of behavior in the 3-CSRTT is thus possible, which is supported by pharmacological studies (Barak and Weiner, 2011). Optogenetic gamma drive of FS-PV neurons in barrel cortex was recently shown to enhance sensory perception (Siegle et al., 2014), and in line with this, we next activated the FS-PV neurons at gamma frequencies. Interestingly, activation of FS-PV neurons at 30–40 Hz during the delay resulted in a decreased rate of errors ($p = 0.01$, paired t test; Figure 7C), with a significant decrease in

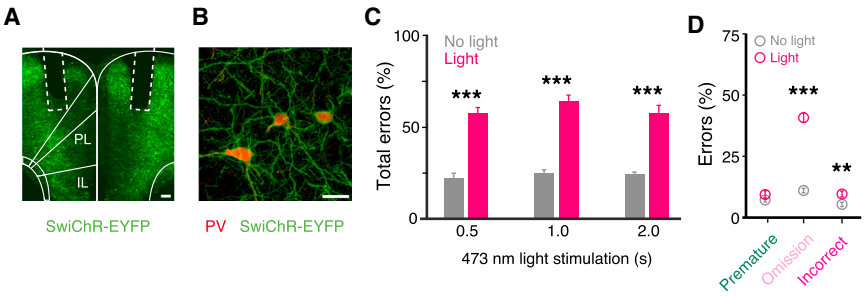

Figure 6. Silencing of mPFC FS-PV Neurons Disrupts Attentional Processing

(A) Placement of bilateral fiber optics and expression of SwiChR-EYFP (green) in mPFC FS-PV neurons in a PV-Cre mouse injected bilaterally with AAV DIO SwiChR-EYFP. 92.9% ± 2.4% of SwiChR-EYFP+ neurons expressed detectable levels of PV (742/802 neurons) and 83.9% ± 1.2% of PV+ neurons expressed SwiChR-EYFP close to the fiber tip (742/886 neurons). n = 5 PV-Cre mice. PL, prelimbic; IL, infralimbic.

(B) PV+ (red) mPFC neurons with SwiChR-EYFP expression (green) and typical PV interneuron morphology.

(C and D) Pseudorandom SwiChR application (red) during the delay in 50% of the trials. Activation: 0.5, 1.0, or 2.0 s of 473 nm in separate sessions; termination: 1 s 638 nm.

(C) Inhibition of mPFC FS-PV neurons during the delay results in more than a doubling of the total number of errors (premature + incorrect + omission) independent of blue light application (0.5, 1.0, or 2.0 s). Total errors: 59.8% ± 10.7% with light, 23.6% ± 6.4% without light; 0.5, 1.0, and 2.0 s combined.

(D) Inhibition of mPFC FS-PV neurons during the delay results in a large increase in the number of omitted trials. Data combined from 0.5, 1.0, and 2.0 s 473 nm light stimulation.

**p < 0.01, ***p < 0.001; error bars, mean ± SEM; Scale bars, (A) 100 μm; (B) 25 μm. See also Figures S5 and S6.

the number of omitted responses (p = 0.01 compared to trials without light, paired t test; Figure 7D), directly demonstrating that gamma synchronization of mPFC FS-PV neurons benefits attentional processing.

The pro-cognitive effects of gamma synchronization of FS-PV neurons were instant, short lasting, and specific to attention. Long-lasting effects are expected to be carried over to the pseudorandomly intermingled trials without light, but they were not (Figure 7C). The 30–40 Hz activation of FS-PV neurons did not affect motivation, as there was no significant difference in reward collection latencies between correct trials with or without light, regardless of the time point, power, or frequency of the light application (Figures S7C–S7E). As with the use of SwiChR, ChR2 application during the delay did not generate motor deficits, as the reaction time was not increased in correct trials with light compared to trials without light (Figures S7F–S7H).

DISCUSSION

Attention guides behavioral responses by selecting task-relevant information for further processing, and the signatures of attention have been extensively studied in sensory systems. Signals of attention arise in PFC (Baluch and Itti, 2011; Buschman and Miller, 2007; Li et al., 2010), a central site for executive control and coordination of goal-driven behavior. Studies in monkeys have consistently identified PFC as a key site for control of attention and a source of attentional modulation of neural responses in downstream brain structures (Clark et al., 2015; Gregoriou et al., 2014; Miller and Buschman, 2013; Moore and Armstrong, 2003; Rossi et al., 2007). However, the circuit underpinnings and mechanisms behind PFC's control of attentional processing have been largely unknown. More specifically, the computations by which PFC could communicate behavioral goals and contribute to selective enhancement of relevant representations in downstream areas have not been demonstrated. Further, a causal link between synchronous brain activity in attention and behavior has been missing (Gregoriou et al., 2015).

mPFC Neural Correlates of Attentional Processing in Goal-Directed Behavior

Our results firmly establish that mPFC FS-PV neurons are recruited by attentional processing and that enhanced and sustained FS-PV spiking predicts successful execution of goal-directed behavior. This surprisingly uniform modulation of mPFC FS-PV neurons constitutes a first cell-type-specific neural correlate of successful allocation of attention. We find that local WS neurons are separated into populations with suppressed or enhanced activity during attentional processing and that this separation is most pronounced during successful allocation of attention, possibly reflecting selective and optimal mPFC integration of the neuronal representations needed for achieving the goal. Our data do not reveal what representations are processed nor their cellular sources. The target and its value, the rules, and the goal of the task engage top-down attention (Clark et al., 2015) and are suggested representations needed to be actively maintained in mPFC during task performance.

The Role of Gamma in Attention

We find that successful allocation of attention is accompanied by elevated mPFC LFP activity in the gamma band and that elevated gamma is coupled to synchronous firing of FS-PV neurons and gamma-phase-dependent silencing of local WS neurons (Cardin et al., 2009). During enhanced gamma, local WS firing also became synchronized (Hasenstaub et al., 2005), supporting the view that gamma rhythm provides a means for formation of assemblies of WS neurons with coordinated firing (Buzsáki and Watson, 2012). Synchronization of pyramidal action potential firing is a proposed mechanism for how gamma rhythmicity could promote the relay of relevant information and drive firing in the proper targets with higher probability (Buzsáki and Watson, 2012; Salinas and Sejnowski, 2000, 2001). This could directly contribute to the preferential processing of task-relevant stimuli in downstream areas (Gregoriou et al., 2014) and, ultimately, to the behavioral benefits of attention.

Our data also suggest that the gamma rhythmic inhibition imposes phase-selective gain modulation of local WS neurons

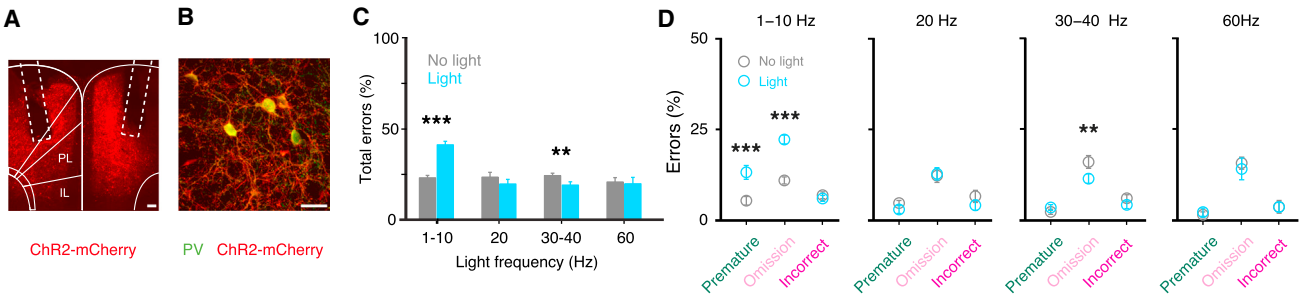

Figure 7. Frequency-Dependent FS-PV Modulation of Attentional Processing

(A) Placement of bilateral fiber optics and expression of ChR2-mCherry (red) in mPFC FS-PV neurons in a PV-Cre mouse injected bilaterally with AAV DIO ChR2-mCherry. 92,9% ± 1.0% of ChR2-mCherry+ neurons expressed PV (670/725 neurons) and 87.7% ± 0.8% of PV+ neurons expressed ChR2-mCherry close to the fiber tip (670/764 neurons); n = 5 PV-Cre mice; PL, prelimbic; IL, infralimbic.

(B) PV+ (green) mPFC neurons with ChR2-mCherry expression (red) and typical PV interneuron morphology.

(C and D) Pseudorandom ChR2 application (473 nm; blue) during the delay in 50% of the trials.

(C) Error rate with (blue) or without (gray) light application. The error rate in trials without light does not differ, regardless of stimulation frequency used in intermingled trials with light (1–10, 20, 30–40, or 60 Hz; $p > 0.1$ one-way ANOVA with repeated measures).

(D) Rate of different error types with (blue) or without (gray) light application. 30–40 Hz drive of FS-PV neurons reduces the number of omitted trials.

$^{**}p < 0.01$, $^{***}p < 0.001$; error bars, mean ± SEM. Scale bars, (A) 100 μm; (B) 25 μm. See also Figure S7.

during attention, which has been anticipated by modeling and optogenetic studies (Cardin et al., 2009; Pritchett et al., 2015; Siegle et al., 2014; Tiesinga et al., 2004, 2008). The cycles of strong FS-PV inhibition create brief time windows with decaying inhibition in the trough of gamma right before onset of the next gamma cycle, where WS neurons would be most sensitive to input and produce maximal output (Womelsdorf et al., 2014). Gamma rhythmic inhibition thus could enhance the throughput of task-relevant information both by synchronization of WS firing and by generating WS output with a higher spike probability. Taken together, our electrophysiological recordings support the view that the temporal conditions created by FS-PV firing specifically in the gamma range support computations underlying top-down control of attention and cognitive behavior (Fries, 2009).

The Role of mPFC PV-FS Neurons in Attention

Our SwiChR experiments show that silencing of mPFC FS-PV neurons during attentional processing has detrimental effects on goal-directed behavior. Based on our electrophysiological findings, it is conceivable that decreased inhibition by FS-PV neurons precludes proper gamma rhythmicity and prevents accurate synchronization and attentional modulation of local WS firing. As discussed, this is expected to impact the formation of WS assemblies and the relay to downstream structures.

While the finding of improved behavior with forced synchronization of mPFC FS-PV neurons at gamma frequencies can seem surprising, gamma oscillations have long been predicted to serve cognition (Gray and Singer, 1989), a concept recently finding direct experimental support. In optogenetic experiments, gamma drive of FS-PV neurons in PFC had pro-cognitive effects and could rescue deficits in cognitive flexibility (Cho et al., 2015). The pro-cognitive effects remained long term, which contrasts the instant and short-lasting effects in our study. Further, while Cho et al. (2015) used drive of gamma to rescue cognitive deficits in a mutant mouse, we demonstrate selective enhancement of attentional processing in overtrained normal mice. It thus appears that prefrontal gamma activity can support various aspects of cognitive processing on multiple timescales and probably through different circuit operations. It will be important for future studies to characterize the computations by which FS-PV gamma mediates particular constructs of cognition and under what contingencies.

The demonstration of frequency-dependent FS-PV modulation of attentional processing is conceptually important for our understanding of how synchronous brain activity can support cognition. This finding also agrees with the idea that oscillations are appropriate targets for investigation of pathophysiology of mental disorders characterized by changed cognition (Buzsáki and Watson, 2012) and, more specifically, that PV neurons play a key role in psychiatry (Hu et al., 2014). The pro-cognitive effects of synchronization of FS-PV neurons at gamma frequencies suggest that cell-type-specific manipulations can be used for enhancement of cortical computations and cognition. This concept is very encouraging, but it also underscores that, in order to understand the operations of the brain, we need to understand the component cells by their functions.

EXPERIMENTAL PROCEDURES

Mice were trained in the 3-CSRTT to attend to and report the location of a brief visual cue presented pseudorandomly in one of three cue/nose-poking holes (Figure S1A). To increase the attentional load, the cue was presented with pseudorandom delays (3, 4, or 5 s) after trial start. Nose-poking into the correct hole resulted in immediate access to reward, while incorrect reports, premature reports, and omitted responses were unrewarded and scored as errors, resulting in a 5 s timeout during which a new trial could not be initiated. Fully trained animals were implanted with microdrives holding tetrodes targeted to mPFC, and chronic recordings were performed over a large number of 3-CSRTT trials for characterization of the recruitment and firing modulation of mPFC neurons during attentional processing. Cell-type classification of local FS-PV and WS neurons was performed by electrophysiological characterizations, and the classification of FS-PV neurons was verified with opto-tagging using ChR2 in freely moving animals. The activity patterns of FS-PV and WS neurons, respectively, were aligned to trial start and cue presentation, and the correlation between

the firing modulation and attentional processing was investigated. To examine population activity, peri-event time histograms (PETHs) for each unit were normalized in *Z* score and averaged across different trials (correct, incorrect, and omission). For examination of how the activities of the FS-PV and WS populations were modulated by attention, we calculated the attentional modulation index (AMI) 1 s before cue onset. To identify inhibitory putative monosynaptic connections from FS-PV to WS cells, we calculated cross-correlations of spike trains for pairs of simultaneously recorded neurons across correct and error trials. To investigate changes in the power of the LFP during attention and presentation of the cue, respectively, the relative power for different frequency bands was calculated and compared between trial types. To investigate the relationship between single-unit activity and LFPs, we performed spike-LFP phase-locking analysis for correct, incorrect, and omitted trials. To determine the instantaneous phase angle of unit spikes relative to gamma oscillations, the phase vector of the filtered LFP was estimated, and the significance of spike-LFP phase locking was tested using circular statistics. The degree of phase locking was evaluated by the length of the mean resultant vector (MRL, range 0–1) and the concentration parameter (κ). Cohorts of fully trained animals were injected with adeno-associated viruses encoding ChR2 or SwiChR for optogenetic in vivo manipulation of FS-PV activity during attentional processing. Light (5 or 7 mW) was delivered pseudorandomly in 50% of the trials of each session. For SwiChR, 0.5, 1.0, or 2.0 s of blue 473 nm light was delivered at trial start and 1.0 s of red 638 nm light directly after termination of the delay. For ChR2, blue light was applied throughout the delay or during the last 2 s of the delay. The inhibitory action of SwiChR was confirmed with acute recordings with silicon probes in anesthetized animals. Statistical differences were determined by paired t tests and ANOVA with repeated measures (for the effects of optogenetic manipulations). More details are given in Supplemental Experimental Procedures.

SUPPLEMENTAL INFORMATION

Supplemental Information includes Supplemental Experimental Procedures, seven figures, and four movies and can be found with this article online at http://dx.doi.org/10.1016/j.cell.2015.11.038.

AUTHOR CONTRIBUTIONS

H.K. modified the 3-CSRTT task and equipment; trained, injected, and implanted the animals; planned and performed the electrophysiological and optogenetic experiments; analyzed and plotted the data; and critically reviewed the manuscript. S.Ä.R aided in training, electrophysiological, and optogenetic experiments and performed histological analysis. X.W. trained animals, and K.D. provided SwiChR, supervised its use, and reviewed the manuscript. M.C. conceived the project, designed the experiments, analyzed the data, wrote the manuscript, and prepared the figures.

ACKNOWLEDGMENTS

We thank H. Shin, C.I. Moore, and K. Meletis for invaluable scientific discussions and H. Yang for the graphical abstract. This work was supported by a European Research Council Starting Grant (337069, M.C.), the Knut and Alice Wallenbergs Foundation (Wallenberg Academy Fellow Grant KAW 2012.0208, M.C.), a Ragnar Söderberg Fellow in Medicine Grant (M.C.), the Swedish Brain Foundation (Hjärnfonden, M.C.), and NIH (K.D).

Received: July 7, 2015
Revised: September 9, 2015
Accepted: November 11, 2015
Published: January 14, 2016

REFERENCES

Amitai, N., and Markou, A. (2010). Disruption of performance in the five-choice serial reaction time task induced by administration of N-methyl-D-aspartate receptor antagonists: relevance to cognitive dysfunction in schizophrenia. Biol. Psychiatry *68*, 5–16.

Atallah, B.V., Bruns, W., Carandini, M., and Scanziani, M. (2012). Parvalbumin-expressing interneurons linearly transform cortical responses to visual stimuli. Neuron *73*, 159–170.

Baluch, F., and Itti, L. (2011). Mechanisms of top-down attention. Trends Neurosci. *34*, 210–224.

Barak, S., and Weiner, I. (2011). Putative cognitive enhancers in preclinical models related to schizophrenia: the search for an elusive target. Pharmacol. Biochem. Behav. *99*, 164–189.

Bari, A., Dalley, J.W., and Robbins, T.W. (2008). The application of the 5-choice serial reaction time task for the assessment of visual attentional processes and impulse control in rats. Nat. Protoc. *3*, 759–767.

Berndt, A., Lee, S.Y., Ramakrishnan, C., and Deisseroth, K. (2014). Structure-guided transformation of channelrhodopsin into a light-activated chloride channel. Science *344*, 420–424.

Buschman, T.J., and Miller, E.K. (2007). Top-down versus bottom-up control of attention in the prefrontal and posterior parietal cortices. Science *315*, 1860–1862.

Buzsáki, G., and Wang, X.J. (2012). Mechanisms of gamma oscillations. Annu. Rev. Neurosci. *35*, 203–225.

Buzsáki, G., and Watson, B.O. (2012). Brain rhythms and neural syntax: implications for efficient coding of cognitive content and neuropsychiatric disease. Dialogues Clin. Neurosci. *14*, 345–367.

Cardin, J.A., Carlén, M., Meletis, K., Knoblich, U., Zhang, F., Deisseroth, K., Tsai, L.H., and Moore, C.I. (2009). Driving fast-spiking cells induces gamma rhythm and controls sensory responses. Nature *459*, 663–667.

Carlén, M., Meletis, K., Siegle, J.H., Cardin, J.A., Futai, K., Vierling-Claassen, D., Rühlmann, C., Jones, S.R., Deisseroth, K., Sheng, M., et al. (2012). A critical role for NMDA receptors in parvalbumin interneurons for gamma rhythm induction and behavior. Mol. Psychiatry *17*, 537–548.

Cho, K.K., Hoch, R., Lee, A.T., Patel, T., Rubenstein, J.L., and Sohal, V.S. (2015). Gamma rhythms link prefrontal interneuron dysfunction with cognitive inflexibility in Dlx5/6(+/-) mice. Neuron *85*, 1332–1343.

Clark, K., Squire, R.F., Merrikhi, Y., and Noudoost, B. (2015). Visual attention: Linking prefrontal sources to neuronal and behavioral correlates. Prog. Neurobiol. *132*, 59–80.

Courtin, J., Chaudun, F., Rozeske, R.R., Karalis, N., Gonzalez-Campo, C., Wurtz, H., Abdi, A., Baufreton, J., Bienvenu, T.C., and Herry, C. (2014). Prefrontal parvalbumin interneurons shape neuronal activity to drive fear expression. Nature *505*, 92–96.

Donnelly, N.A., Paulsen, O., Robbins, T.W., and Dalley, J.W. (2015). Ramping single unit activity in the medial prefrontal cortex and ventral striatum reflects the onset of waiting but not imminent impulsive actions. Eur. J. Neurosci. *41*, 1524–1537.

Fries, P. (2009). Neuronal gamma-band synchronization as a fundamental process in cortical computation. Annu. Rev. Neurosci. *32*, 209–224.

Fujisawa, S., Amarasingham, A., Harrison, M.T., and Buzsáki, G. (2008). Behavior-dependent short-term assembly dynamics in the medial prefrontal cortex. Nat. Neurosci. *11*, 823–833.

Gold, J.M., Fuller, R.L., Robinson, B.M., Braun, E.L., and Luck, S.J. (2007). Impaired top-down control of visual search in schizophrenia. Schizophr. Res. *94*, 148–155.

Gray, C.M., and Singer, W. (1989). Stimulus-specific neuronal oscillations in orientation columns of cat visual cortex. Proc. Natl. Acad. Sci. USA *86*, 1698–1702.

Gregoriou, G.G., Gotts, S.J., Zhou, H., and Desimone, R. (2009). High-frequency, long-range coupling between prefrontal and visual cortex during attention. Science *324*, 1207–1210.

Gregoriou, G.G., Rossi, A.F., Ungerleider, L.G., and Desimone, R. (2014). Lesions of prefrontal cortex reduce attentional modulation of neuronal responses and synchrony in V4. Nat. Neurosci. *17*, 1003–1011.

Gregoriou, G.G., Paneri, S., and Sapountzis, P. (2015). Oscillatory synchrony as a mechanism of attentional processing. Brain Res. *1626*, 165–182.

Hangya, B., Pi, H.J., Kvitsiani, D., Ranade, S.P., and Kepecs, A. (2014). From circuit motifs to computations: mapping the behavioral repertoire of cortical interneurons. Curr. Opin. Neurobiol. *26*, 117–124.

Hasenstaub, A., Shu, Y., Haider, B., Kraushaar, U., Duque, A., and McCormick, D.A. (2005). Inhibitory postsynaptic potentials carry synchronized frequency information in active cortical networks. Neuron *47*, 423–435.

Hayden, B.Y., Smith, D.V., and Platt, M.L. (2009). Electrophysiological correlates of default-mode processing in macaque posterior cingulate cortex. Proc. Natl. Acad. Sci. USA *106*, 5948–5953.

Hu, H., Gan, J., and Jonas, P. (2014). Interneurons. Fast-spiking, parvalbumin^{+} GABAergic interneurons: from cellular design to microcircuit function. Science *345*, 1255263.

Isomura, Y., Harukuni, R., Takekawa, T., Aizawa, H., and Fukai, T. (2009). Microcircuitry coordination of cortical motor information in self-initiation of voluntary movements. Nat. Neurosci. *12*, 1586–1593.

Kepecs, A., and Fishell, G. (2014). Interneuron cell types are fit to function. Nature *505*, 318–326.

Korotkova, T., Fuchs, E.C., Ponomarenko, A., von Engelhardt, J., and Monyer, H. (2010). NMDA receptor ablation on parvalbumin-positive interneurons impairs hippocampal synchrony, spatial representations, and working memory. Neuron *68*, 557–569.

Kvitsiani, D., Ranade, S., Hangya, B., Taniguchi, H., Huang, J.Z., and Kepecs, A. (2013). Distinct behavioural and network correlates of two interneuron types in prefrontal cortex. Nature *498*, 363–366.

Lee, S.H., Kwan, A.C., Zhang, S., Phoumthipphavong, V., Flannery, J.G., Masmanidis, S.C., Taniguchi, H., Huang, Z.J., Zhang, F., Boyden, E.S., et al. (2012). Activation of specific interneurons improves V1 feature selectivity and visual perception. Nature *488*, 379–383.

Lewis, D.A., Curley, A.A., Glausier, J.R., and Volk, D.W. (2012). Cortical parvalbumin interneurons and cognitive dysfunction in schizophrenia. Trends Neurosci. *35*, 57–67.

Li, L., Gratton, C., Yao, D., and Knight, R.T. (2010). Role of frontal and parietal cortices in the control of bottom-up and top-down attention in humans. Brain Res. *1344*, 173–184.

Lustig, C., Kozak, R., Sarter, M., Young, J.W., and Robbins, T.W. (2013). CNTRICS final animal model task selection: control of attention. Neurosci. Biobehav. Rev. *37* (9 Pt B), 2099–2110.

Marín, O. (2012). Interneuron dysfunction in psychiatric disorders. Nat. Rev. Neurosci. *13*, 107–120.

Miller, E.K., and Buschman, T.J. (2013). Cortical circuits for the control of attention. Curr. Opin. Neurobiol. *23*, 216–222.

Moore, T., and Armstrong, K.M. (2003). Selective gating of visual signals by microstimulation of frontal cortex. Nature *421*, 370–373.

Noudoost, B., Chang, M.H., Steinmetz, N.A., and Moore, T. (2010). Top-down control of visual attention. Curr. Opin. Neurobiol. *20*, 183–190.

Pritchett, D.L., Siegle, J.H., Deister, C.A., and Moore, C.I. (2015). For things needing your attention: the role of neocortical gamma in sensory perception. Curr. Opin. Neurobiol. *31*, 254–263.

Robbins, T.W. (2002). The 5-choice serial reaction time task: behavioural pharmacology and functional neurochemistry. Psychopharmacology (Berl.) *163*, 362–380.

Rossi, A.F., Bichot, N.P., Desimone, R., and Ungerleider, L.G. (2007). Top down attentional deficits in macaques with lesions of lateral prefrontal cortex. J. Neurosci. *27*, 11306–11314.

Roux, L., and Buzsáki, G. (2015). Tasks for inhibitory interneurons in intact brain circuits. Neuropharmacology *88*, 10–23.

Roux, L., Stark, E., Sjulson, L., and Buzsáki, G. (2014). In vivo optogenetic identification and manipulation of GABAergic interneuron subtypes. Curr. Opin. Neurobiol. *26*, 88–95.

Sachidhanandam, S., Sreenivasan, V., Kyriakatos, A., Kremer, Y., and Petersen, C.C. (2013). Membrane potential correlates of sensory perception in mouse barrel cortex. Nat. Neurosci. *16*, 1671–1677.

Salinas, E., and Sejnowski, T.J. (2000). Impact of correlated synaptic input on output firing rate and variability in simple neuronal models. J. Neurosci. *20*, 6193–6209.

Salinas, E., and Sejnowski, T.J. (2001). Correlated neuronal activity and the flow of neural information. Nat. Rev. Neurosci. *2*, 539–550.

Siegle, J.H., Pritchett, D.L., and Moore, C.I. (2014). Gamma-range synchronization of fast-spiking interneurons can enhance detection of tactile stimuli. Nat. Neurosci. *17*, 1371–1379.

Sohal, V.S., Zhang, F., Yizhar, O., and Deisseroth, K. (2009). Parvalbumin neurons and gamma rhythms enhance cortical circuit performance. Nature *459*, 698–702.

Stark, E., Eichler, R., Roux, L., Fujisawa, S., Rotstein, H.G., and Buzsáki, G. (2013). Inhibition-induced theta resonance in cortical circuits. Neuron *80*, 1263–1276.

Tiesinga, P.H., Fellous, J.M., Salinas, E., José, J.V., and Sejnowski, T.J. (2004). Inhibitory synchrony as a mechanism for attentional gain modulation. J. Physiol. Paris *98*, 296–314.

Tiesinga, P., Fellous, J.M., and Sejnowski, T.J. (2008). Regulation of spike timing in visual cortical circuits. Nat. Rev. Neurosci. *9*, 97–107.

Totah, N.K., Kim, Y.B., Homayoun, H., and Moghaddam, B. (2009). Anterior cingulate neurons represent errors and preparatory attention within the same behavioral sequence. J. Neurosci. *29*, 6418–6426.

Totah, N.K., Jackson, M.E., and Moghaddam, B. (2013). Preparatory attention relies on dynamic interactions between prelimbic cortex and anterior cingulate cortex. Cereb. Cortex *23*, 729–738.

Vinck, M., Womelsdorf, T., Buffalo, E.A., Desimone, R., and Fries, P. (2013). Attentional modulation of cell-class-specific gamma-band synchronization in awake monkey area v4. Neuron *80*, 1077–1089.

Wilson, N.R., Runyan, C.A., Wang, F.L., and Sur, M. (2012). Division and subtraction by distinct cortical inhibitory networks in vivo. Nature *488*, 343–348.

Womelsdorf, T., Valiante, T.A., Sahin, N.T., Miller, K.J., and Tiesinga, P. (2014). Dynamic circuit motifs underlying rhythmic gain control, gating and integration. Nat. Neurosci. *17*, 1031–1039.

Zhang, S., Xu, M., Kamigaki, T., Hoang Do, J.P., Chang, W.C., Jenvay, S., Miyamichi, K., Luo, L., and Dan, Y. (2014). Selective attention. Long-range and local circuits for top-down modulation of visual cortex processing. Science *345*, 660–665.

Cell

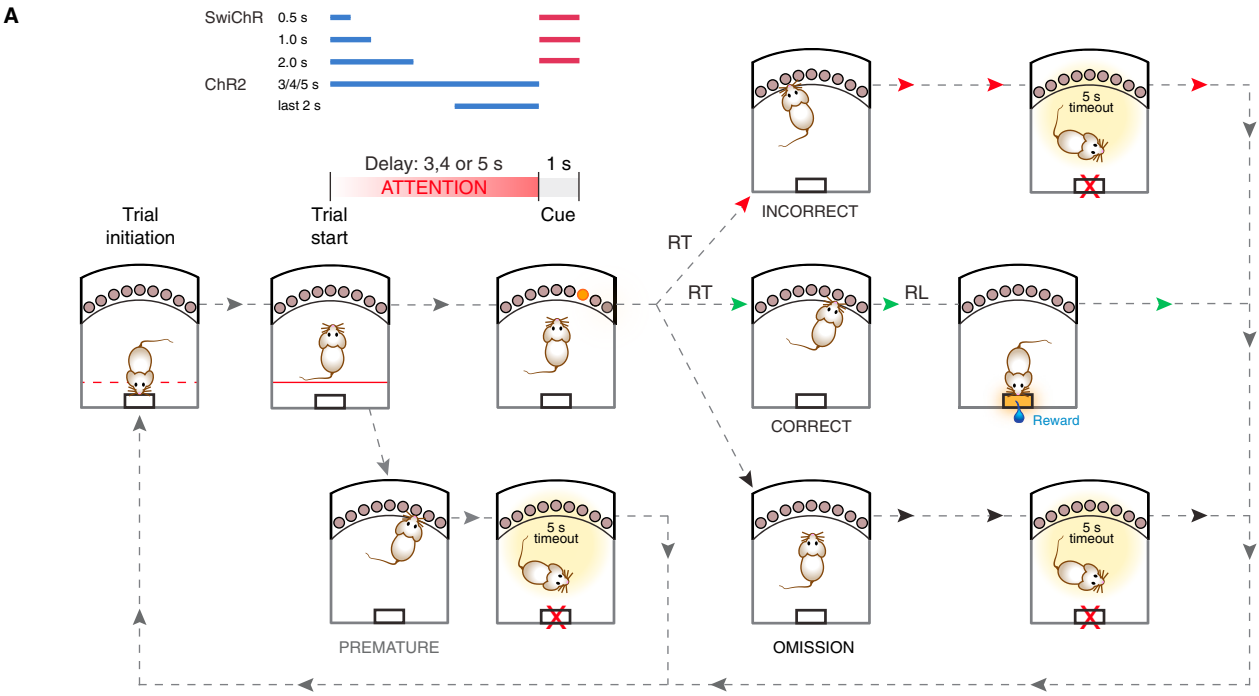

B

Level	Delay (s)	Cue (s)	Max response time (s)*	Progression criteria**
1	2	30	30	≥ 30 correct trials
2	2	20	20	
3	5	10	10	≥ 40 correct trials
4	5	5	5	≥ 50 correct trials ≥ 80% accuracy
5	3/4/5	2	5	≥ 50 correct trials ≥ 80% accuracy
6	3/4/5	1	5	≤ 20% omissions
	3/4/5	1	5	Recordings or optogenetics

* Max response time = Limited hold
** For all levels the progression criteria had to be met for two consecutive days for progression to the next level.

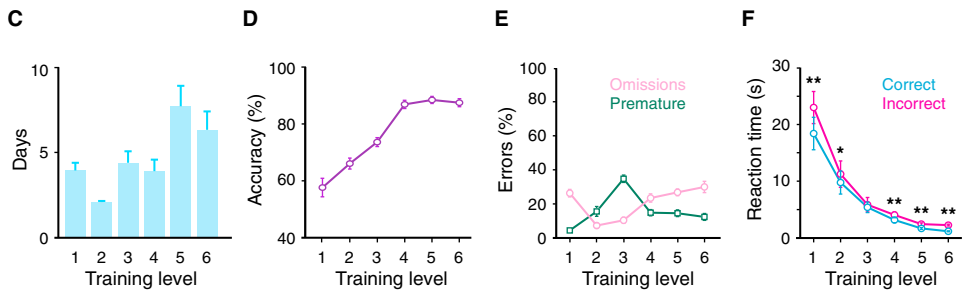

Figure S1. 3-CSRTT: Outline, Optogenetic Applications, and Training, Related to Figure 2

(A) The 3-CSRTT for fully trained animals. From left to right: In order to allow the animals to optimally attend to the presentation of the cue we modified the task and the equipment. Each trial was initiated by pushing of the reward port, but the trial was not started until the animal had turned to face the cue presentation holes (for details see Supplemental Experimental Procedures and Movies S1-S4). Trial start marked the start of the pseudorandom delay (delay = time from trial start to cue onset; 3, 4 or 5 s). Compared to commonly used 5-CSRTT protocols our strategy streamlines the behavior during the delay. The cue (1 s visual stimulus) was presented pseudorandomly in one of three cue presentation holes directly after the delay. Nose-poking into the cue presentation hole (= correct response, Movie S1) resulted in immediate access to reward (15% sucrose solution) in the reward port. Time from cue onset to nose-poke response defined the reaction time (RT). Time from correct nose-poke response to first nose-poke into the reward port defined the reward collection latency (RL). Nose-poking into any of the cue presentation holes before cue onset (premature response, Movie S2) canceled cue presentation. Nose-poke response in any nose-poke hole other than the cue presentation hole defined an incorrect response (Movie S3). The reaction times for incorrect responses were also recorded. Failure to respond within 5 s after cue onset (i.e., limited hold = 5 s) defined an omitted trial (omission; Movie S4). Premature, incorrect and omitted responses resulted in a 5 s timeout during which a new trial could not be initiated.

Optogenetics. Inhibition of FS-PV activity during attention: SwiChR was activated pseudorandomly in 50% of the trials by 0.5, 1.0 or 2.0 s (separate sessions) of 473 nm blue light upon trial start. SwiChR was deactivated by application of 1 s red light (638 nm) after ending of the pseudorandom delay. Activation of FS-PV neurons during attention: ChR2 was activated by blue light (473 nm at different frequencies) throughout the pseudorandom delay or during the last 2 s of the delay.

(B) Training in the 3-CSRTT. The animals were trained at six levels defined by specific criteria. The criteria of each level had to be met for two consecutive days for progression to the next level. After successfully reaching the target criteria (= level 6, two consecutive days with $\geq$ 50 correct trials, $\geq$ 80% accuracy and $\leq$ 20% omissions; pseudorandom delay (3, 4 or 5 s), 1 s cue, 5 s maximum response time) the animals were subjected to chronic electrophysiological recordings or optogenetic manipulations.

(C–F) Training data for the animals used; n = 13 PV-Cre mice (3 chronic recordings during behavior + 5 SwiChR during behavior + 5 ChR2 during behavior). Data represent average performance during each training level.

(C) The average number of days (i.e., sessions) spent at each training level.

(legend continued on next page)

(D) Development of accuracy (number of correct trials / (number of correct trials + number of incorrect trials)) during training.
(E) Number of premature and omitted responses during the different training levels.
(F) The reaction time for correct and incorrect responses during training. Correct responses are consistently faster than incorrect responses (paired t test).
*$p < 0.05$, **$p < 0.01$; error bars, mean ± SEM.

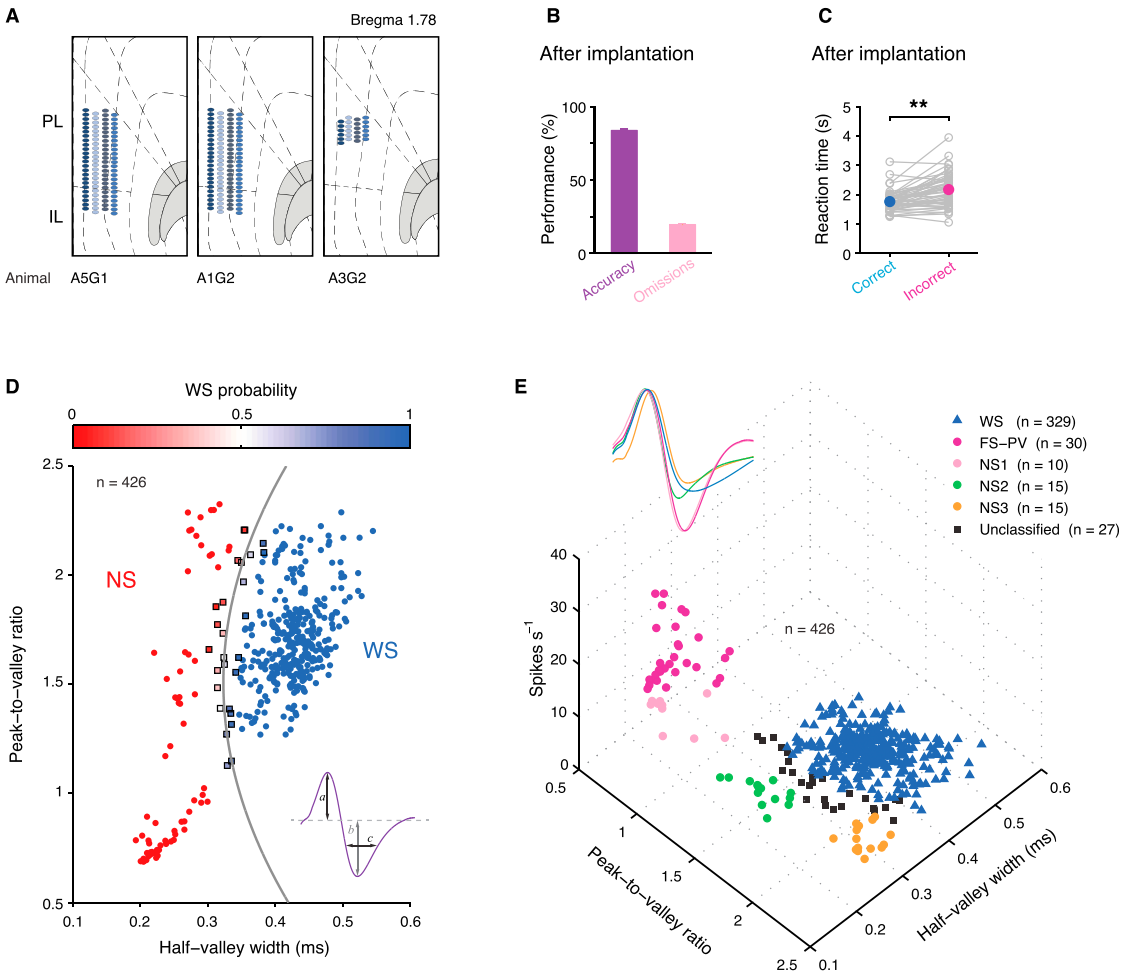

Figure S2. Chronic Electrophysiological Recordings during 3-CSRTT and Cell Type Classifications, Related to Figure 1

(A–E) Data from 3 PV-Cre mice.

(A) Schematic reconstruction of the recording sites.

(B) Performance in the 3-CSRTT during in vivo recordings. (n = 54 sessions). The animals still met the target criteria after implantation of microdrives.

(C) The reaction times are slightly longer after implantation (compare to e.g., Figures S6D, S6E, and S7F–S7H), most likely due to the animals' movement being more restricted by the microdrive than by implanted fibers. The pattern of correct responses showing faster reaction times than incorrect responses remains intact ($p < 0.01$, paired t test).

(D) Units (n = 426) were classified as NS (n = 70, red) or WS (n = 329, blue) based on spike waveform features (half-valley width and peak-to-valley ratio). A Gaussian mixture model (GMM) was used for objective classification of units. 27 units were not classified due to low classification confidence (squares; $p > 0.05$). Inset; the peak (*a*), valley (*b*) and half-valley width (*c*) for a schematic neuron.

(E) Neurons classified on the basis of three electrophysiological properties: the peak-to-valley ratio, the half-valley width and the spike rate. This identified 7.0% (30/426) of the neurons as FS-PV neurons (peak-to-valley ratio < 1.1 and firing rate > 10 Hz; purple). NS neurons with peak-to-valley ratio < 1.1 and firing rate $\leq$ 10 Hz were classified as NS1 (10/426, 2.3%; pink) and the remaining NS neurons as NS2 (15/426, 3.5%; green) or NS3 (15/426, 3.5%; yellow) based on distinct clustering. Blue triangles; WS neurons (326/426, 77.2%), black squares; unclassified neurons (27/426, 6.3%). Inset: representative spike waveforms of the classified neurons.

**$p < 0.01$; error bars, mean ± SEM.

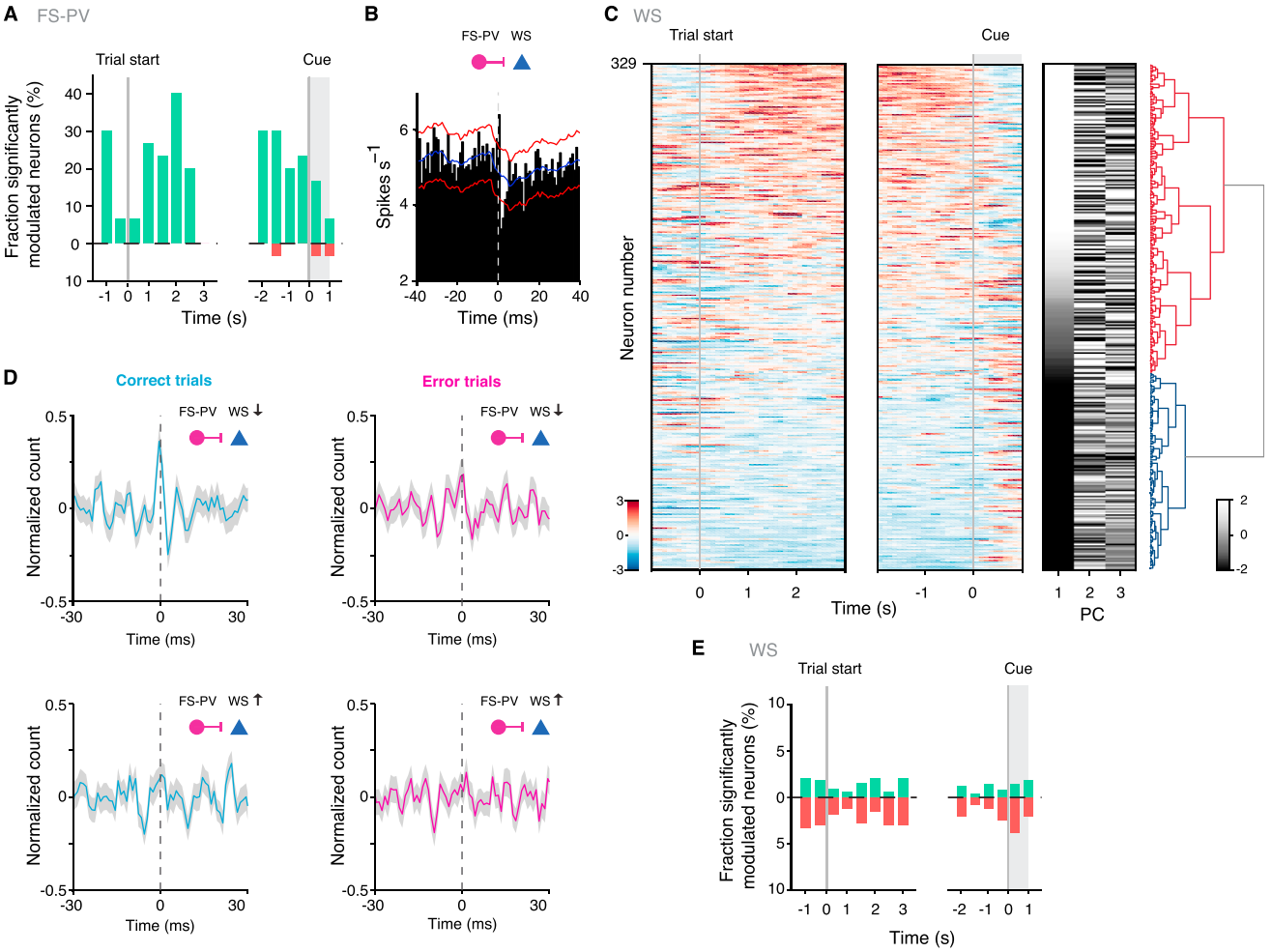

Figure S3. Modulation of and Interactions between FS-PV and WS Neurons during Attentional Processing, Related to Figure 2

(A) The FS-PV neurons (n = 30) homogenously display sustained elevation of activity during successful allocation of attention, with up to 40% of the neurons being significantly modulated ($p < 0.05$, Wilcoxon rank-sum test, 0.5 s time bins). Green, increased activity in correct trials; red, increased activity in error (incorrect + omission) trials.

(B) FS-PV neurons were physiologically characterized by their fast and putative monosynaptic inhibitory interactions with WS neurons. Example of cross-correlogram of spike trains between a FS-PV–WS pair showing short-latency suppression of WS spiking. Blue line denotes mean of time-jittered spikes (1,000 times, randomly within 5 ms) and red lines indicate the 95% confidence interval ($p < 0.05$) from the jittered spikes. We confirmed inhibitory interactions between 21/30 (70%; two or more bins exceeded the lower confidence interval within 10 ms) of the FS-PV neurons and concurrently recorded WS neurons.

(C) Responses (left) and clustering (right) of the individual WS neurons (n = 329) based on their firing modulation during the delay in correct trials. PC = principal component.

(D) Normalized z-score cross-correlograms of short-latency interactions between 53 pairs of FS-PV neurons and WS neurons with suppressed activity (WS↓), and between 55 pairs of FS-PV neurons and WS neurons with enhanced activity (WS↑) during the delay of correct and error (incorrect + omission) trials (WS ≥ 100 spikes over all trials). The fastest and strongest FS-PV inhibition is seen in correct trials, targeting the WS neurons with suppressed activity. Shaded area; SEM.

(E) The WS neurons display mixed modulations during attention (significantly modulated neurons: $p < 0.05$, Wilcoxon rank-sum test, 0.5 s time bins). Colors as in (A).

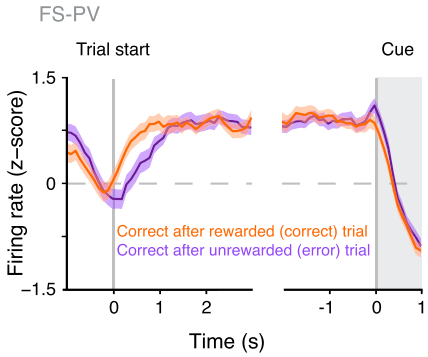

Figure S4. FS-PV Activity in Relation to Prior Behavior, Related to Figure 3

Data from correct trials. PETH aligned to trial start and to cue onset showing the activity of all FS-PV neurons (n = 30), 500 ms sliding window, 100 ms time bins. The result of the behavior in the previous trial does not affect the level of FS-PV activation in a directly subsequent correct trial. The timing of recruitment was however significantly different, with the FS-PV neurons being recruited earlier if the previous trial was rewarded ($p < 0.01$, paired t test). 1 s after trial start there was no difference in the FS-PV activity regardless if the previous trial was rewarded or not. Shaded areas; SEM.

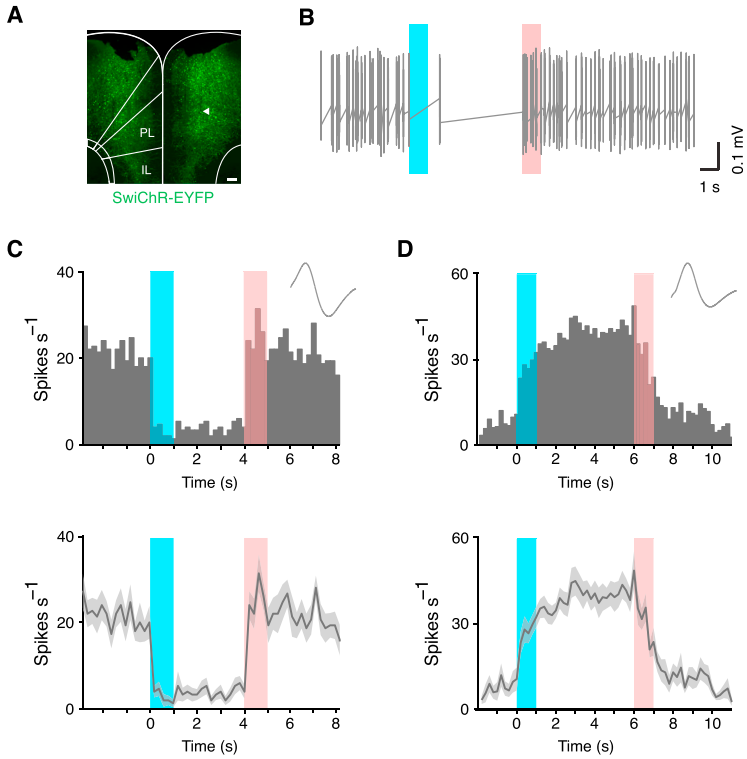

Figure S5. SwiChR Conveys Fast and Bistable Inhibition of mPFC FS-PV Neurons In Vivo, Related to Figure 6

(A) To confirm the bistable inhibitory action of the chloride channel SwiChR in mPFC FS-PV neurons in vivo, AAV DIO SwiChR-EYFP (green) was injected into mPFC of PV-Cre mice (n = 4). Arrowhead points to example track mark from the silicon probe, the probe tip was targeted to PL. For labeling specificity and efficiency see Figure 6A-B.

(B–D) Blue light (1 s, 473 nm, 5 mW; blue bar) and red light (1 s, 638 nm, 5 mW; red bar) were applied at different intervals during acute anesthetized recordings.

(B) Example trace of bistable spiking modulation of a mPFC FS-PV neuron. Application of blue light resulted in fast and sustained inhibition of spiking. Spiking resumed very rapidly after red light application.

(C) Top; PSTH of bistable inhibition of a FS-PV neuron aligned to blue light onset, n = 15 trials. Inset; representative spike waveform, with typical FS-PV features. Bottom; average modulation of the neuron. Shaded area; SEM.

(D) Top; PSTH aligned to blue light onset of bistable disinhibition of a neuron in the local mPFC circuitry recorded concurrently to the inhibited FS-PV neurons in (C), n = 15 trials. Inset; representative spike waveform. Bottom; average modulation of the neuron. Shaded area; SEM.

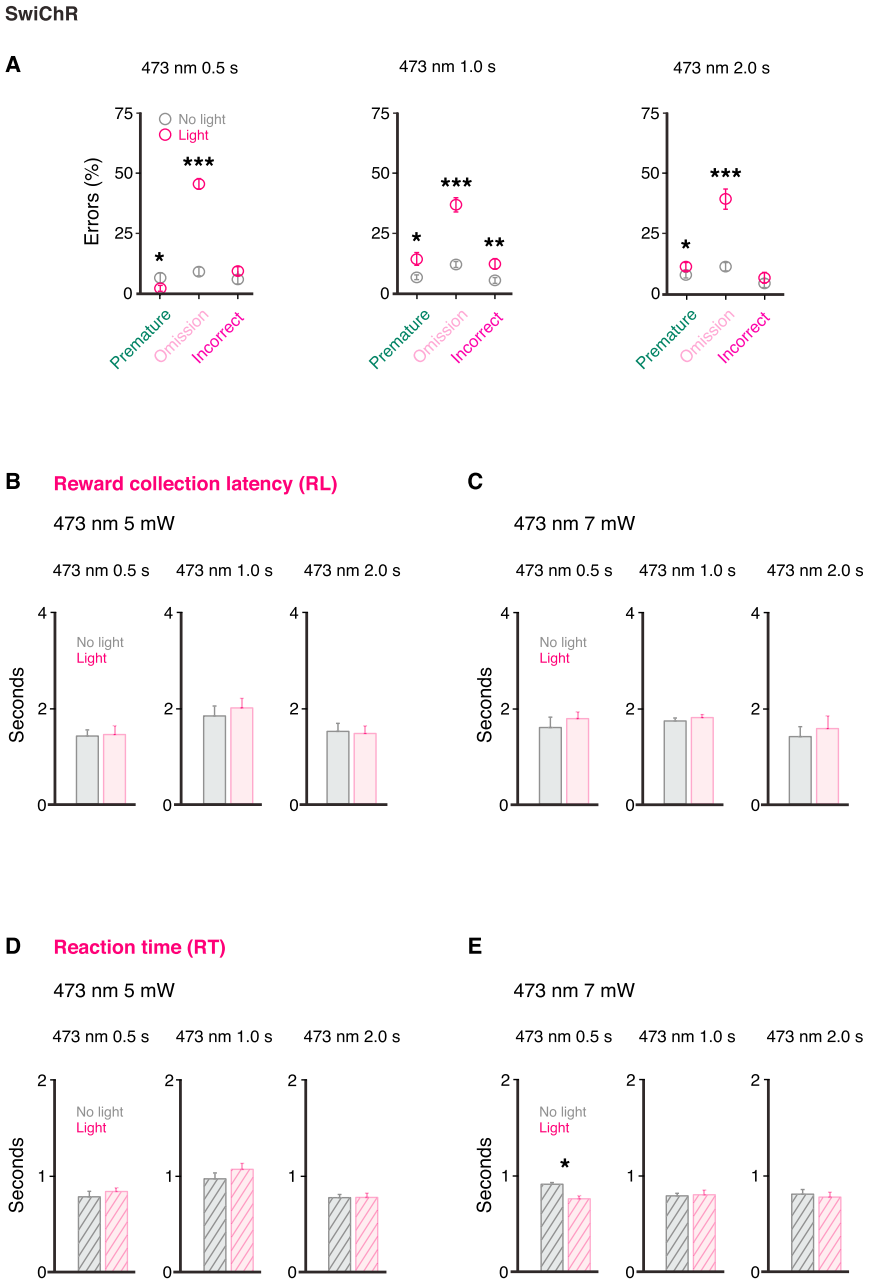

Figure S6. The Effects of SwiChR Activation on Attentional Processing, Reward Latencies, and Reaction Times, Related to Figure 6

(A–E) SwiChR activation was applied pseudorandomly in 50% of the trials in every session. Activation: 0.5, 1.0 or 2.0 s 473 nm blue light in separate sessions, termination: 1 s 638 nm red light in all trials with SwiChR application. n = 5 PV-Cre mice.

(A) Error types for each SwiChR stimulation paradigm used.

(B–E) Data from correct trials.

(B and C) Optogenetic silencing of FS-PV neurons during attentional processing did not affect the latency to collect reward (i.e., there was no difference in reward collection latencies (RL) in trials with light compared to trials without light), regardless of blue light-pulse duration and light intensity ($p > 0.05$, three-way ANOVA with repeated-measures followed by Tukey's post hoc test).

(D–E) Optogenetic silencing of FS-PV neurons during attentional processing did not increase the reaction time (RT; time from cue onset to nose-poke response), regardless of blue light-pulse duration and light intensity ($p > 0.05$, three-way ANOVA with repeated-measures followed by Tukey's post hoc test).

*$p < 0.05$, **$p < 0.01$, ***$p < 0.001$; error bars, mean ± SEM.

ChR2 473 nm, 5 mW last 2 s of the delay

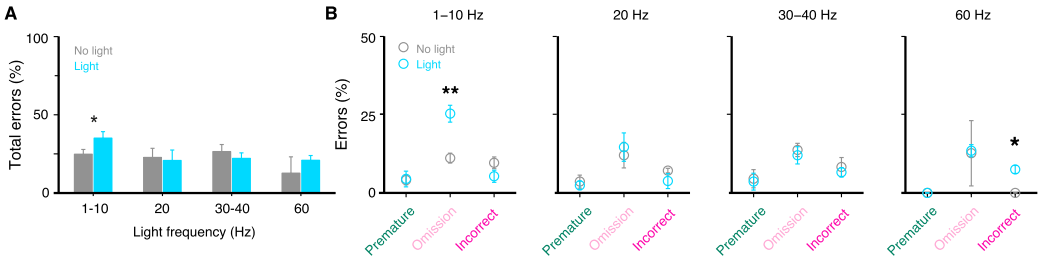

Reward collection latency (RL)

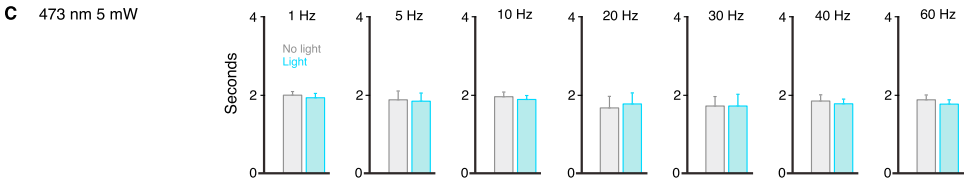

Reaction time (RT)

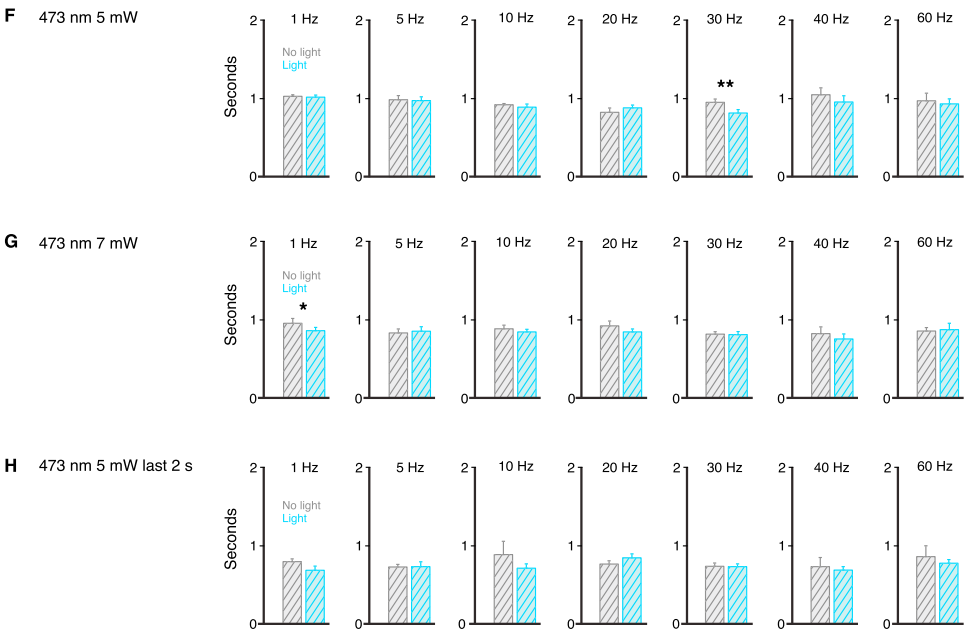

(legend on next page)

Figure S7. The Effects of ChR2 Activation on Attentional Processing, Reward Latencies, and Reaction Times, Related to Figure 7

(A–H) n = 5 PV-Cre mice.

(A–B) ChR2 activation of FS-PV neurons was restricted to the last 2 s (−2 to 0 s) of the delay pseudorandomly in 50% of the trials (473 nm, 5 mW).

(A) Optogenetic activation of mPFC FS-PV neurons at low frequencies (1-10 Hz) resulted in a significant increase in the total numbers of errors (premature + incorrect + omission, $p < 0.05$, paired t test). Activation at 20 Hz did not affect the error rate ($p = 0.86$, paired t test). Activation at 30-40 Hz did not result in a significant decrease in the numbers of errors, which could potentially be explained by insufficient number of sessions (1 sessions compared to 6 sessions of optogenetic activation throughout the delay, compare to Figure 7C).

(B) Optogenetic activation of mPFC FS-PV neurons at 1-10 Hz resulted in a significant increase in the number of omitted trials ($p < 0.01$, t test).

(C–H) Data from correct trials. ChR2 activation (473 nm, blue) was applied pseudorandomly in 50% of the trials in every session.

(C–E) Optogenetic activation of FS-PV neurons during attentional processing did not affect the latency to collect reward (i.e., there was no difference in reward collection latencies (RL) in trials with light compared to trials without light) regardless of light intensity, stimulation frequency, or timing of light application ($p > 0.05$, three-way ANOVA with repeated-measures followed by Tukey's post hoc test).

(F–H) Optogenetic activation of FS-PV neurons during attentional processing did not increase the reaction time (RT; time from cue onset to nose-poke response) regardless of light intensity, stimulation frequency, or timing of light application ($p > 0.05$, three-way ANOVA with repeated-measures followed by Tukey's post hoc test).

*$p < 0.05$, **$p < 0.01$; error bars, mean ± SEM.

Cell

Supplemental Information

Prefrontal Parvalbumin Neurons in Control of Attention

Hoseok Kim, Sofie Ährlund-Richter, Xinming Wang, Karl Deisseroth, and Marie Carlén

Supplemental Experimental Procedures

Animals

All procedures were performed in accordance with the Guidelines of the Stockholm municipal committee for animal experiments. Adult (8-10 weeks old at start of any experiment) PV-Cre (Hippenmeyer et al., 2005) male mice were used in all experiments. The animals were housed under 12:12H light:dark cycles. For animals used in the 3-CSRTT the daily amount of food was restricted to 1 g of food per 10 g body weight until the animals reached 85% of their free-feeding weight at what point training in the 3-CSRTT began. The animals were kept on food restriction throughout all sessions in the 3-CSRTT.

Behavior

In the 3-CSRTT the animals allocate attention to report the location of a visual stimulus in order to receive reward. The 3-CSRTT operant chambers (CeNeS, UK) were equipped with one house light on each of the two sidewalls and nine stimulus (cue) presentation nose poke holes with internal light-emitting diodes and an infrared sensor detecting the insertion of the animals' nose on the front wall, of which three were used. The reward port holding the reward magazine and an infrared sensor detecting the insertion of the animals' nose was situated on the rear wall. The animals were habituated to the experimenter and the operant chambers for 7 days before training. The animals were trained in 6 successive training levels defined by specific criteria (**Figure S1B**) and the criteria of each level had to be met for two consecutive days for progression to the next level. Every animal was trained in all four operant 3-

CSRTT chambers, one chamber per session and one session per day. A session was terminated after 100 trials or after 60 minutes if not 100 trials were executed.

Each trial was initiated and started by the animal's behavior (see further below). In order to increase the attentional load (Robbins, 2002) the visual cue was presented pseudorandomly 3, 4 or 5 seconds after trial start (stimulus onset asynchrony). The pseudorandom delay (delay; time from trial start to cue onset, often referred to as the inter trial interval (ITI) in 5-CSRTT studies) was introduced in training level 5 and used in all trials with recordings or optogenetics. A nose poke into a cue presentation hole within 5 s after cue onset (limited hold) defined the behavioral response (correct; Movie S1 or incorrect; Movie S3) and the reaction time (RT; time from cue onset to first registered nose poke, i.e. the response latency). Correct report of the cue location resulted in immediate access to reward (15% sucrose solution) in the reward port. Time from cue report to first pushing of the reward port in a correct trial defined the reward latency (RL). Failure to report the cue location within the limited hold (5 s for fully trained animal used in recordings and optogenetics) was scored as an omitted trial (omission; Movie S4), and a nose poke response before cue presentation as a premature response (Movie S2). Incorrect, premature and omitted responses resulted in a 5 second illuminated timeout. During this time a new trial could not be initiated.

After correct report of cue location the animal rapidly turns around, pushes the reward port with the nose and consumes reward (**Movie S1**). In the commonly used 5-CSRTT protocol (Bari et al., 2008) a nose poke into the reward port also leads to initiation of a new trial. In essence, reward port nose poke starts the delay and automatically triggers onset of the cue after a defined time interval (often 5 s). In a correct trial the animal thus must consume reward, turn around and successfully

allocate sufficient attention to the cue presentation holes within 5 s in order to be able to correctly report the cue location. In an error trial the animal awaits the termination of the illuminated 5 s timeout (**Movie S2-S4**), pushes the reward port to initiate a new trial and turns to the cue presentation holes to attend to the upcoming cue. In summary, in the commonly used protocol pushing of the reward port results in temporal differences in the behavior during the delay depending on if the previous trial was rewarded or not. To circumvent these discrepancies and to streamline the behavior during the delay (i.e. assure that the behavior and neural activity recorded during the delay reflects attentional processing in all trials), we equipped the chambers with an infrared photobeam running between the sidewalls in front of the reward port (**Figure S1A**). Approaching of the reward port broke the beam and while the pushing of the reward port defined trial initiation after both correct and error trials, reward port pushing did not start of the delay. Instead, the delay was not started until the animal had left the reward port and turned to face the cue presentation holes, an event defined by release of the beam break (**Movie S1-S4**).

All sessions were videotaped and reviewed for elimination of trials where the animals did not behave stereotypically, i.e. trials where the animal unexpectedly did not attend to the cue presentation holes. These trials were not used in any type of analysis.

Microdrive construction and implantation

For chronic *in vivo* electrophysiology we employed the flexDrive (Voigts et al., 2013), a small size (~2 cm height, ~1.5 cm diameter) and low weight (~2 g) system which allows for independent day-to-day positioning of tetrodes for large-scale and long-term recordings of single neurons in the brain. Tetrodes consisted of four twisted fine

wires (polyimide insulated ni-chrome wire, 12 μm, Sandvik-Kanthal) that were gold-plated to reduce the impedance to 0.2-0.4 MΩ at 1 kHz. Four movable tetrodes were loaded into medical-grade polyimide carrier tubes (0.005 inch OD, Phelps Dodge) in the microdrive.

The animals were anaesthetized with isoflurane (2%) in O_2 and the body temperature maintained at 37° with a temperature controller system. The animals were fixed in a stereotaxic frame and a hole was drilled through the skull (1.76 mm anterior to Bregma, and 0.25 mm lateral to midline). The microdrive was positioned above the craniotomy and gradually lowered to the PL area (1.25 mm ventral to brain surface). Four miniature anchoring screws were used to attach the microdrive to the skull (two on the anterior and two on the posterior part of the scull). Two Teflon-coated stainless steel wires (0.005 inch bare, A-M systems) from the electrode interface board (EIB) of the microdrive were connected to the screws for grounding. The microdrive was secured onto the skull using dental adhesive cement (Super Bond C&B, Sun Medical). The animals were injected with analgesic (Buprenorphine 0.1 mg/kg s.c.) at the end of surgery and thereafter single-housed.

Chronic electrophysiological recordings during 3-CSRTT

3 fully trained PV-Cre mice were implanted with a flexDrive (Voigts et al., 2013) (1 animal in left hemisphere, and 2 animals in right hemisphere, for details see *Microdrive construction and implantation*). The animals were allowed to recover and acclimate to the microdrive for 7 days and thereafter re-trained in the 3-CSRTT for 7-14 days to assure continued performance at the target criteria.

The neural activity was recorded in a total of 54 3-CSRTT sessions using a Digital Lynx 4SX acquisition system and the Cheetah data acquisition software

(Neuralynx). 3,857 trials were recorded (64-100 trials / session). The tetrodes were individually lowered 20-40 μm after every recording session. Unit signals were amplified with the gain of 10,000, filtered with bandwidth 600-6,000 Hz, digitized at 32 kHz, and stored on a PC. Local field potentials (LFPs) were acquired from one electrode of each tetrode at a sampling rate of 32 kHz. The signal was band-pass filtered between 0.1 and 500 Hz. The last recording day the final position of each tetrode was marked with electrolytic lesion and the animals were thereafter perfused. The tetrode tracks were reconstructed using histological analysis.

Data analysis. All data analysis was conducted using custom software written in MATLAB (Math Works).

Unit sorting

Single units were manually sorted and identified by various spike waveform features (energy, peak, area, spike width, principal components, and fast Fourier transform) using MClust offline sorter (A.D. Redish). Only well-isolated units (Schmitzer-Torbert et al., 2005) with isolation distance > 15, L-ratio < 0.2, and the spikes < 0.01% at ISI < 2 ms were included in the data analysis.

Unit classification

The units were first classified into wide-spiking (WS) putative pyramidal neurons and narrow-spiking (NS) putative interneurons based on the distribution of (1) the peak-to-valley ratio (the ratio between the amplitude of the initial peak (*a*) and the following trough (*b*)) and (2) the half-valley width (*c*) of each spike waveform. For objective classification of units, a Gaussian mixture model (GMM) was fit to the units

(Stark et al., 2013). Units with low classification confidence ($P > 0.05$) were not classified.

To identify putative FS-PV interneurons, the NS population was further classified based on firing rate (data from all trials). NS neurons with a peak-to-valley ratio < 1.1 and a mean firing rate > 10 Hz were classified as FS-PV neurons. NS neurons with peak-to-valley ratio > 1.1 and mean firing rate ≤ 10 Hz were classified as NS1 neurons and the remaining NS neurons as NS2 or NS3 based on distinct clustering.

To evaluate the similarity between optically tagged FS-PV neurons and FS-PV neurons recorded during 3-CSRTT we compared **a,** spike shapes and **b,** cluster distance between the opto-tagged FS-PV neurons and the four classes of NS neurons (FS-PV, NS1-3). Normalized cross-correlation (*r*) values between spike waveforms were calculated to quantify waveform similarity (Jackson and Fetz, 2007). The value of 1 indicates identical spike waveforms. For Mahalanobis distances a lower value indicates higher similarity.

Optogenetic identification of FS-PV interneurons (opto-tagging) during active behavior

For *in vivo* optical tagging of FS-PV neurons 4 PV-Cre mice were injected with AAV DIO ChR2-mCherry (Cardin et al., 2009, 2010) (for details see *Viral injections*) and implanted with the flexDrive (Voigts et al., 2013) (2 animals in left hemisphere, and 2 animals in right hemisphere). The microdrives were equipped with a 200 μm multimode optical fiber (numeric aperture (NA) 0.22, Thorlabs) and 4 movable tetrode wires were positioned in carrier tubes in a circular pattern around the optical fiber. Electrophysiological recordings from the PL/IL were initiated 2-4 w after viral

injection and the tetrodes were lowered individually 20-40 μm after every recording session (for details see *Microdrive construction and implantation* and *Chronic electrophysiological recordings during 3-CSRTT*). Light (5-10 mW at the tip of the fiber, 3-5 ms light pulses, 10-90 Hz) was delivered from a DPSS blue laser (Cobolt MLD^{TM} 473 nm, Cobolt) controlled by custom software written in LabVIEW.

We recorded a total of 252 single units from PL and IL during active behavior (a total of 46 sessions from 4 animals). To identify directly light-activated FS-PV interneurons we employed an automated, unsupervised optical-tagging test (Stimulus-Associated spike Latency Test, SALT) (Kvitsiani et al., 2013). Using SALT it is possible to statistically determinate whether the timing of spikes is significantly changed in relation to the onset of optogenetic activation for identification of directly activated neurons displaying short latency spikes with low jitter. To ensure that the spike sorting was not compromised by light-application, the waveforms of light evoked and spontaneous spike were compared using Pearson's correlation coefficient. Using these measures (SALT P-value < 0.01, Pearson's correlation coefficient $r > 0.9$) 12 units were identified as FS-PV interneurons (half-valley width 248 ± 21 μs, mean firing rate 22 ± 8 Hz) and used for comparison to FS-PV neurons recorded during 3-CSRTT.

Temporal dynamics of neuronal activity during attention

Peri-event time histograms (PETHs) of the firing rate of each FS-PV and WS unit were calculated by a 500 ms sliding window in 100 ms steps with the relevant task events (trial start and cue onset) at time 0 across all trials. To examine population activity PETHs for each unit were normalized in z-score and averaged across different trials (correct, incorrect, and omission). To estimate the probability of spike

occurrence over time, we computed a mean spike density function (SDF) using a Gaussian kernel of 100 ms.

WS clustering

For WS cell sub-classification, we first calculated PCA (principal component analysis) scores using the singular value decomposition of the z-scores of firing rate during the delay of correct trials. Unsupervised hierarchical clustering (Ward's method) was thereafter performed using the first three PCs of the z-scores. Based on the clustering, WS cells were separated into 2 sub-populations, one with increased and one with decreased firing during attention.

Attentional modulation index (AMI)

To quantify how the FS-PV and WS neurons were modulated by attention we computed the AMI (Treue and Maunsell, 1999) by comparing for each neuron the responses 1 s (-1 to 0 s) before cue onset for correct and error trials (FRcorr-FRerror)/(FRcorr+FRerror). AMI ranges from -1 to 1. Positive values represent enhanced spiking in correct trials, negative values enhanced spiking in error trials. The value is zero if there is no modulation.

Cross-correlation analysis

To identify inhibitory putative monosynaptic connections and short-latency interactions between FS-PV and WS cells, we calculated cross-correlations of spike trains for pairs of simultaneously recorded neurons across correct and error trials using a bin size of 1 ms. Only units recorded from different tetrodes were included in the analysis to avoid artificial troughs at time 0. The cross-correlation values were

normalized by dividing by the number of spikes of the reference cell. We used a jittering method to estimate the expected cross-correlogram with 95% confidence interval (Fujisawa et al., 2008). For each cell pair the spikes of one spike train were jittered 1,000 times randomly in the [-5, 5] ms interval. Significant troughs within 10 ms of the center bin were considered to be due to inhibition only when two or more bins were below the 95% confidence interval. For averages of FS-PV--WS pairs, cross-correlograms were standardized by subtracting the mean and dividing by the standard deviation of the jittered cross-correlograms.

Relationship between FS-PV activity and the reaction time (RT)

For investigation of the correlation between the FS-PV activity during attention and the reaction time we compared the firing rate of all FS-PV neurons 1 s (-1 to 0 s, 1 s epoch) before cue onset to the response latency in all correct trials (response latency = time from cue onset to nose poke response, i.e. the reaction time). To remove a potential confounding effect of time, residual values were obtained by subtracting the mean firing rate and reaction time from each value on a trial-by-trial basis (Janssen and Shadlen, 2005). We then calculated the correlation coefficient (r) using these residual values for each cell. Fast and slow RTs: RTs faster than the median reaction time were defined as fast RTs and RT slower than the median as slow RTs (Hayden et al., 2009).

Spectral analysis

Local field potential (LFP) signals were processed in Matlab. The signals were down-sampled to 1 kHz and LFP power spectrum was computed using the Chronux toolbox (*mtspectrumc*). LFP power spectrograms (20-100 Hz) were constructed using the

continuous wavelet transform (complex Morlet wavelet, *cmor1.5-1* in the Matlab wavelet toolbox) and normalized by the peak power. To investigate the relative power of the LFP during attentional processing (-2 to 0 s before cue onset) and cue period (0 to 1 s after cue onset) the power within the band of interest (5-10, 12-24, 30-40 and 60-80 Hz) was divided by the total power of frequencies in the 1-100 Hz range and averaged across trials.

Phase locking analysis

To investigate the relationship between single-unit activity and local field potentials during attentional processing we performed spike-LFP phase locking analysis based on the behavioral outcome (correct, incorrect, omission) the last 2 s of the delay (-2 to 0 s before cue onset). Only neurons with ≥ 50 spikes during the period analysed were used for phase locking estimation. First, the LFP signal (recorded from the same tetrode as single units) was band-pass filtered (30-40 Hz) using the *eegfilt* function from the EEGLAB toolbox. The phase vector of the filtered LFP was then estimated using the Hilbert transform and the mean spike-gamma phase angle for each unit thereafter calculated. We tested the significance of spike-LFP phase locking using circular statistics (CirStat toolbox for Matlab). Rayleigh test was used to assess the circular distribution of the mean phase angle of neurons and to test the non-uniformity of each neuron's spike phase distribution to gamma. The neurons were considered significantly phase-locked if $P < 0.05$. Phase-locking of populations of FS-PV and WS neurons was evaluated by calculation of the concentration parameter (κ) and the length of the mean resultant vector (MRL, range 0-1) of the spike-gamma phase angle distribution of a population. A MRL value of 1 indicates exact phase synchrony, whereas a value of 0 indicates no phase synchrony. A larger value of kappa (κ)

indicates smaller circular variance of the mean spike-gamma phase angles of the neurons in the population. The mean phase angle (μ) was computed as the circular direction of the MRL.

Viral injections

The animals were anaesthetized with isoflurane (2%) in O_2 and the body temperature maintained at 37° with a temperature controller system. The animals were fixed in a stereotaxic frame and a small craniotomy was made 1.76 mm anterior to Bregma, and 0.25 mm lateral to midline, unilaterally for opto-tagging and bilaterally for characterization of SwiChR *in vivo* and optogenetic manipulation during behavior. The virus was delivered by a glass capillary attached to a motorized stereotaxic injector (Stoelting) at 0.1 μl min^{-1} and the center of the injection was targeted to PL (AP 1.76 mm, LM ± 0.25 mm, DV -1.3). The pipette was held in place for 5 min after injection before being slowly retracted from the brain. The incision was closed with tissue glue (Vetbond, 3M) and the animals were injected with analgesic (buprenorphine 0.1 mg/kg s.c.) at the end of surgery.

For opto-tagging and optogenetic activation of FS-PV neurons the adeno-associated viral vector AAV DIO ChR2-mCherry (Cardin et al., 2009) (pAAV-Ef1A-DIO-hChR2(H132R)-mCherry-WPRE-pA, for vector outline see www.optogenetics.org) was used (0.6 μl for opto-tagging, 0.4 μl / hemisphere for optogenetic activation during behavior, 1x10e11-1x10e12 viral particles / ml).

For inhibition of FS-PV neurons the adeno-associated viral vector AAV DIO SwiChR-EYFP (Berndt et al., 2014) (pAAV-EF1A-DIO $SwiChR_{CA}$-TS-EYFP-WPRE, for vector outline see www.optogenetics.org) was used (0.4 μl / hemisphere, 4x10e12 viral particles / ml).

Characterization of the inhibitory action of SwiChR *in vivo*

To characterize the inhibitory action of SwiChR (Berndt et al., 2014) *in vivo,* animals (4 PV-Cre mice) were injected bilaterally with the adeno-associated viral vector AAV DIO SwiChR-EYFP (for details see *Viral injections*). 4-5 weeks later the animals were anaesthetized with isoflurane (2%) in O_2. The body temperature was maintained at 37° with a temperature controller system. The animals were fixed in a stereotaxic frame and a small craniotomy was made 1.76 mm anterior to Bregma, and 0.25 mm lateral to midline. For the acute recordings 32-channel silicon probes (4 shanks with 2 tetrodes, NeuroNexus) and a Digital Lynx 4SX acquisition system with Cheetah data acquisition software (Neuralynx) were used. The silicon probe was targeted to PL/IL and light (5 mW at the fiber tip) was delivered via an optical fiber (200 µm) placed at the surface of the target brain area. The optical fiber was connected to a patch cable (Doric Lenses) coupled to a blue DPSS laser (Cobolt MLD^{TM} 473 nm, Cobolt) and a red DPSS laser (Cobolt MLD^{TM} 638 nm, Cobolt) controlled by custom software written in LabVIEW. 1 s blue light was delivered and 1 s red light was used to terminate SwiChR activation 3, 4 or 5 s later.

Optogenetics during behavior

Inhibition of FS-PV neurons during attentional processing in the 3-CSRTT

The animals (5 PV-Cre mice) were habituated to the experimenter and the operant chambers for 7 days and thereafter injected bilaterally with the adeno-associated viral vector AAV DIO SwiChR-EYFP (for details see *Viral injections*). After 7 days of recovery the animals started training in the 3-CSRTT. After fulfilling the criteria of level 5 the animals were implanted with optical fibers for optogenetic application. In brief, the animals were anaesthetized with isoflurane (2%) in O_2 and the body

temperature maintained at 37° with a temperature controller system. The animals were fixed in a stereotaxic frame and a small craniotomy was made bilaterally 1.76 mm anterior to Bregma, and 0.25 mm lateral to midline. Optical fibers (200 µm, 0.22 NA) with ceramic ferrules (1.25 mm ID, Precision Fiber Products (PFP)) were bilaterally implanted (10° angle) in mPFC. Two anchoring screws were attached in the skull (one in the left frontal and the other in the right parietal bone) to achieve better fixation of the dental cement. UV cured dental cement (Tetric EvoFlow, Ivoclar Vivadent) with adhesion primer (Optibond FL, Kerr) was used to secure the optic ferrules on the skull. After implantation, the optical fibers were covered with custom-made protectors to keep the fiber cores clean and good in condition. The incision was closed with tissue glue (Vetbond, 3M). The animals were injected with analgesic (buprenorphine 0.1 mg/kg s.c.) at the end of surgery and thereafter single-housed. After 7 days of recovery the animals continued training in the 3-CSRTT and after fulfilling the criteria of level 6 optogenetic application was initiated.

Light was delivered *via* a fiber optic rotary joint/patch cable system (Doric Lenses) coupled to a blue DPSS laser (Cobolt MLD^{TM} 473 nm, Cobolt) and a red DPSS laser (Cobolt MLD^{TM} 638 nm, Cobolt) controlled by custom software written in LabVIEW. The fiber optic cable was connected to the implants using ceramic ferrule sleeves and the connection between the patch cable and the implanted optic fiber was completely covered with heat shrink tubing to prevent visualization of the light from becoming a cue to the animals. 0.5, 1.0 or 2.0 s blue light (different sessions; 5 or 7 mW at the fiber tip) was delivered at trial start pseudorandomly in 50% of the trials (4,362 trials in total from 5 animals). Thus in every session 50% of the trials were no light trials for comparison to the trials with light in that specific session. SwiChR activation was terminated with 1 s red light directly after ending of

the pseudorandom delay at all occasions.

Activation of FS-PV neurons during attentional processing in the 3-CSRTT

The animals (5 PV-Cre mice) were habituated to the experimenter and the operant chambers for 7 days and thereafter injected bilaterally with the adeno-associated viral vector AAV DIO ChR2-mCherry (Cardin et al., 2009) (for details see *Viral injections*). After 7 days of recovery the animals started training in the 3-CSRTT. After fulfilling the criteria of level 5 the animals were implanted with optical fibers for optogenetic application. In brief, the animals were anaesthetized with isoflurane (2%) in O_2 and the body temperature maintained at 37° with a temperature controller system. Optical fibers (200 µm, 0.22 NA) with ceramic ferrules (1.25 mm ID, Precision Fiber Products (PFP)) were bilaterally implanted (10° angle) in mPFC. Two anchoring screws were attached in the skull (one in the left frontal and the other in the right parietal bone) to achieve better fixation of the dental cement. UV cured dental cement (Tetric EvoFlow, Ivoclar Vivadent) with adhesion primer (Optibond FL, Kerr) was used to secure the optic ferrules on the skull. After implantation, the optical fibers were covered with custom-made protectors to keep the fiber cores clean and good in condition. The incision was closed with tissue glue (Vetbond, 3M). The animals were injected with analgesic (buprenorphine 0.1 mg/kg s.c.) at the end of surgery and thereafter single-housed. After 7 days of recovery the animals continued training in the 3-CSRTT and after fulfilling the criteria of level 6 optogenetic application was initiated.

Light was delivered *via* a fiber optic rotary joint/patch cable system (Doric Lenses) coupled to a blue DPSS laser (Cobolt MLD^{TM} 473 nm, Cobolt) controlled by custom software written in LabVIEW. The fiber optic cable was connected to the

implants using ceramic ferrule sleeves and the connection between the patch cable and the implanted optic fiber was completely covered with heat shrink tubing to prevent visualization of the light from becoming a cue to the animals. 5 ms blue light (5 or 7 mW at the fiber tip in different sessions) was delivered at different frequencies (1, 5, 10, 20, 30, 40, 60 Hz, one frequency per session) throughout the delay or during the last 2 s of the delay pseudorandomly in 50% of the trials (10,302 trials in total from 5 animals). Thus in every session 50% of the trials were no light trials for comparison to the trials with light in that specific session.

Anatomical analysis

The mice were deeply anesthetized with pentobarbital and transcardially perfused using 100 mM PBS followed by 4% paraformaldehyde in PBS. Brains were carefully removed and postfixed in 4% paraformaldehyde in PBS for 18h at 4°C. After thorough washing in PBS the entire PFC was sectioned (50 μm thickness) using a vibratome (Leica VT1000, Leica Microsystems).

Targeting of electrodes and optical fibers to PL/IL was confirmed using microscopy (Leica DM6000B fluorescent microscope with a Hamamatsu Orca-FLASH 4.0 C11440 digital camera at 16-bit depth resolution) and anatomical reconstructions (Allen brain atlas, Allen Institute).

For specificity and efficacy of opsin labeling every second 50 μm brain slice were collected for staining. The sections were incubated in blocking solution (0.3% Triton X100 and 10% Normal Donkey Serum in 1x TBS) for 2H followed by incubation with primary antibody (1:1000 rabbit anti Parvalbumin, PV25, Swant) for 18h in room temperature. After washing the sections were incubated with a species-

specific fluorophore conjugated secondary antibody (1:1000 goat anti-rabbit Cy5, Jackson) for 2H, washed, mounted on glass slides and coverslipped.

The specificity and efficacy of opsin labeling was score by hand around identified sites of fiber optic placements (3 sections / animal, n = 5 SwiChR injected PV-Cre mice and 5 ChR2 injected PV-Cre mice) using a Leica DM6000B fluorescent microscope with a Hamamatsu Orca-FLASH 4.0 C11440 digital camera at 16-bit depth resolution. Images were acquired (20x magnification) and individual cells were examined for the presence of PV and/or opsin labeling.

Statistical analysis. Statistical significance was tested with t-test, ANOVA, or Wilcoxon rank sum test. All values are expressed as mean ± s.e.m. unless noted otherwise.

Supplemental References

Bari, A., Dalley, J.W., and Robbins, T.W. (2008). The application of the 5-choice serial reaction time task for the assessment of visual attentional processes and impulse control in rats. Nature protocols *3*, 759-767.

Berndt, A., Lee, S.Y., Ramakrishnan, C., and Deisseroth, K. (2014). Structure-guided transformation of channelrhodopsin into a light-activated chloride channel. Science *344*, 420-424.

Cardin, J.A., Carlen, M., Meletis, K., Knoblich, U., Zhang, F., Deisseroth, K., Tsai, L.H., and Moore, C.I. (2009). Driving fast-spiking cells induces gamma rhythm and controls sensory responses. Nature *459*, 663-667.

Cardin, J.A., Carlen, M., Meletis, K., Knoblich, U., Zhang, F., Deisseroth, K., Tsai, L.H., and Moore, C.I. (2010). Targeted optogenetic stimulation and recording of neurons in vivo using cell-type-specific expression of Channelrhodopsin-2. Nature protocols *5*, 247-254.

Fujisawa, S., Amarasingham, A., Harrison, M.T., and Buzsaki, G. (2008). Behavior-dependent short-term assembly dynamics in the medial prefrontal cortex. Nature neuroscience *11*, 823-833.

Hayden, B.Y., Smith, D.V., and Platt, M.L. (2009). Electrophysiological correlates of default-mode processing in macaque posterior cingulate cortex. Proceedings

of the National Academy of Sciences of the United States of America *106*, 5948-5953.

Hippenmeyer, S., Vrieseling, E., Sigrist, M., Portmann, T., Laengle, C., Ladle, D.R., and Arber, S. (2005). A developmental switch in the response of DRG neurons to ETS transcription factor signaling. PLoS biology *3*, e159.

Jackson, A., and Fetz, E.E. (2007). Compact movable microwire array for long-term chronic unit recording in cerebral cortex of primates. Journal of neurophysiology *98*, 3109-3118.

Janssen, P., and Shadlen, M.N. (2005). A representation of the hazard rate of elapsed time in macaque area LIP. Nature neuroscience *8*, 234-241.

Kvitsiani, D., Ranade, S., Hangya, B., Taniguchi, H., Huang, J.Z., and Kepecs, A. (2013). Distinct behavioural and network correlates of two interneuron types in prefrontal cortex. Nature *498*, 363-366.

Robbins, T.W. (2002). The 5-choice serial reaction time task: behavioural pharmacology and functional neurochemistry. Psychopharmacology *163*, 362-380.

Schmitzer-Torbert, N., Jackson, J., Henze, D., Harris, K., and Redish, A.D. (2005). Quantitative measures of cluster quality for use in extracellular recordings. Neuroscience *131*, 1-11.

Stark, E., Eichler, R., Roux, L., Fujisawa, S., Rotstein, H.G., and Buzsaki, G. (2013). Inhibition-induced theta resonance in cortical circuits. Neuron *80*, 1263-1276.

Treue, S., and Maunsell, J.H. (1999). Effects of attention on the processing of motion in macaque middle temporal and medial superior temporal visual cortical areas. The Journal of neuroscience : the official journal of the Society for Neuroscience *19*, 7591-7602.

Voigts, J., Siegle, J.H., Pritchett, D.L., and Moore, C.I. (2013). The flexDrive: an ultra-light implant for optical control and highly parallel chronic recording of neuronal ensembles in freely moving mice. Frontiers in systems neuroscience *7*, 8.